

**Hydrogen Embrittlement of Additively Manufactured
Austenitic Stainless Steel 316L**

K.M. Bertsch, A. Nagao, B. Rankouhi, B. Kuehl, D. Thoma

Hydrogen embrittlement of additively manufactured austenitic stainless steel 316L

K.M. Bertsch^{1,2,3*}, A. Nagao⁴, B. Rankouhi⁵, B. Kuehl¹, D.J. Thoma^{1,2}

¹Department of Materials Science and Engineering, University of Wisconsin-Madison, 1550 Engineering Dr., WI 53706, USA

²Grainger Institute for Engineering, University of Wisconsin-Madison, Madison, WI 53706, USA

³Lawrence Livermore National Laboratory, Livermore, CA 94550, USA

⁴International Institute for Carbon-Neutral Energy Research (WPI-I2CNER), Kyushu University, 744 Moto-oka, Nishi-ku, Fukuoka, Fukuoka 819-0395, Japan

⁵Department of Mechanical Engineering, University of Wisconsin-Madison, 1550 Engineering Dr., WI 53706, USA

Author email addresses:

* Corresponding author: K. M. Bertsch, bertsch5@llnl.gov +1(925)423-7995

A. Nagao, akihidenagao@gmail.com

B. Rankouhi, rankouhi@wisc.edu

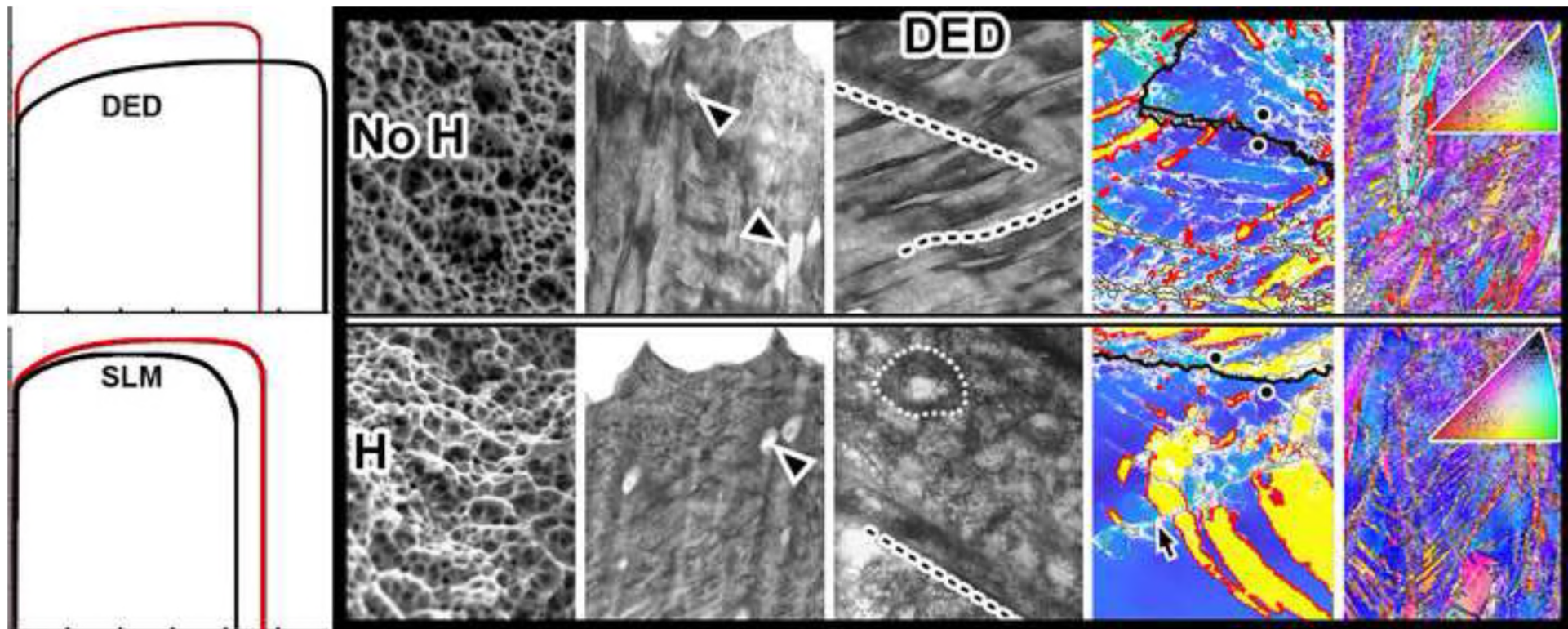
B. Kuehl, bkuehl2@wisc.edu

D. J. Thoma, dthoma@wisc.edu

Keywords: Additive manufacturing, Hydrogen embrittlement, Dislocations, Stainless steel, Transmission electron microscopy

Highlights

- Stainless steels additively manufactured with different methods exposed to hydrogen
- Hydrogen reduced ductility in only as-built directed energy deposited material
- Hydrogen enhanced dislocation cells and texture in directed energy deposited material
- Hydrogen interactions with dislocations, segregation, and precipitates are explored
- Hydrogen-dislocation interactions appear most closely linked to tensile response



Abstract

Additive manufacturing (AM) is a promising means of production of austenitic stainless steel (SS) parts for hydrogen service. The hydrogen embrittlement resistance of SS 316L parts manufactured by powder-bed-fed selective laser melting (SLM) and directed energy deposition (DED) was examined using slow strain rate tensile testing. The influence of the hierarchical AM microstructures on mechanical response, microstructural evolution, and void formation were analyzed using multiscale electron microscopy. The presence of hydrogen reduced ductility in as-built DED materials, but did not significantly influence the response in as-built SLM material or heat-treated materials. Microstructural features driving these different responses are discussed.

1. Introduction

The presence of hydrogen in a metal can reduce the macroscopic ductility and cause a transition to a less ductile failure mode in a phenomenon known as hydrogen embrittlement (HE). Despite the long history of study of this phenomenon, questions remain regarding the exact mechanism driving the negative influence of hydrogen on mechanical properties [1-6]. Accordingly, phenomenological exploration and testing are always required to determine the influence of composition and microstructure on hydrogen environment compatibility and also to deregulate the existing conservative selection of materials suitable for use for hydrogen applications.

Stainless steels (SSs), particularly stable austenitic SS series such as type 316, 316L or 310S, have been found to be relatively resistant to HE [7-13], which is frequently attributed to their reduced formation of strain-induced α' or ϵ martensite and low hydrogen diffusivity [2]. This resistance makes stable austenitic SSs excellent candidates for hydrogen environment applications such as high-pressure hydrogen gas pressure vessels, piping, valves, and hoses for use in hydrogen refueling stations, as well as in the petrochemical industry [14]. However, these stable austenitic SS have comparably low strength relative to other advanced low-alloy steels, especially in the solution-treated condition [14, 15], leading to thicker walled structures or components and greater expense. This can be particularly an obstacle in the realization of the sustainable hydrogen economy, which will rely on hydrogen gas pressures in excess of 70 MPa to achieve acceptable efficiencies [16-18]. To compensate for these shortcomings, cold working can be used. The effects of the microstructure induced by cold work on susceptibility to HE has been studied in austenitic SS [12, 14, 19-21], however, this effect has not been fully elucidated due to insufficient data including its underlying mechanism [2]. Thus, it is desirable to find more ways to increase the strength of these materials for use in service environments of hydrogen.

Additive manufacturing (AM) technologies, consisting of layer-by-layer deposition of molten metals for rapid fabrication, have attracted substantial research interest due to the increased design flexibility afforded by the technique [22]. AM SS exhibit dislocation densities in the range of cold-worked steels and have been reported to show enhanced strength and ductility simultaneously [22-29]. The enhanced behavior has been attributed to the distinctive, hierarchical AM microstructures comprising dendritic segregation patterns, dislocation cells, and precipitates, all of which can vary depending on AM method [7, 19, 30, 31]. This unique enhanced balance between strength and ductility of AM materials indicates potential suitability for hydrogen service environments.

The compatibility of AM SS materials with hydrogen environments has not been extensively studied [32], attracted recent research interest. In metastable SS type 304L, tensile testing in a hydrogen gas environment has suggested superior HE resistance in AM 304L material due to decreased martensite formation compared to conventional rolled SS 304L [33]. Strain-induced martensite formation has been indicated to be suppressed in selective laser melting (SLM) AM 316L, suggested to be due to the dense, cellular dislocation structure in AM material [34]. Furthermore, electrochemical testing was suggested to induce less martensite transformation and surface damage in SLM 316L compared to wrought 316L material [35]. However, while correlations between austenite stability and HE resistance have been observed, several studies have indicated that the relationship is indirect and not sufficient to account for HE resistance of austenitic steels [10, 36, 37]. This evidence suggests that the susceptibility of AM material to HE should be discussed not only with well-established martensite transformation but also with a new perspective. Further, the variation depending on specimen microstructure indicates that it remains

critical to evaluate the suitability of material made with different AM processes on a case-by-case basis.

In this experiment, the influence of AM processing on the susceptibility to HE was investigated as a function of both the initial microstructure and the microstructural evolution in the absence of martensite transformation. Two different AM methods, powder-bed-fed SLM and directed energy deposition (DED), were used to fabricate SS type 316L components with different microstructures for testing in the absence and presence of hydrogen. As-built and heat-treated parts made using both methods were subjected to slow strain rate tensile (SSRT) tests in uncharged and hydrogen-charged states to evaluate the effect of the AM microstructures on the susceptibility to HE.

2. Materials and Methods

2.1 Manufacturing and processing

An EOS M290 powder-bed unit was used to fabricate SLM parts. In powder-bed SLM, components are produced by scanning a laser over a stationary bed of powder to melt each layer. The component is moved down between successive layers and new powder is swept across the bed to build parts layer-by-layer. In this study, standard print parameters recommended by EOS were used to fabricate SLM parts, with laser power 195 W, scan speed 1083 mm/s, layer thickness 20 μm , and hatch spacing 90 μm . More details regarding the laser scan strategy and other process parameters are reported in Rankouhi et al. [38]. SS 316L powder provided by EOS was used with powder particle size less than 60 μm .

Separately, an Optomec Laser Engineered Net Shaping (LENS) MR-7 unit was used to fabricate DED parts. In DED processes, a laser is used to melt a substrate and powder is expelled from a nozzle into the melt pool. The substrate is moved beneath the stationary laser to continuously deposit material in each layer. In the present study, DED components were printed with laser power 275 W, scan speed 8.5 mm/s, layer thickness 254 μm , and hatch spacing 350 μm . The LENS MR-7 laser spot size was approximately 700 μm . Additional details regarding powder feed rate, scan strategy, and other process parameters are reported in Rankouhi et al. [38]. These components were printed as rectangular bars 50 mm long x 10 mm wide and approximately 3 mm thick. All samples were made with the shortest dimension in the build direction and the longest dimension in the plane of the build plate [38]. Parts were printed using SS 316L powder for the LENS supplied by Carpenter[®]. The Carpenter powder particle size ranged from 45 to 150 μm .

Several important differences between the processes include: cooling rate, which can be orders of magnitude higher in SLM processes compared to DED [39]; laser size, which creates different melt pool and minimum feature sizes; residual stress, which tends to be higher in SLM components; heat flow; and input energy density [22, 32, 40, 41]. These variations can create significant differences in microstructural features such as porosity, grain size, dislocation structure, and second phases, all of which can affect the material response to environmental degradation such as corrosion or hydrogen embrittlement [32, 41]. Microstructural differences between SLM and DED materials used in the current study are discussed in Section 2.2.

Electrical discharge machining (EDM) was used first to remove parts from the build plates, then subsequently to machine them into tensile specimen geometry. Tensile specimen gauge sections were 25 mm long x 6 mm wide x approximately 3 mm thick; thickness of SLM and DED specimens was 3.0-3.5 and 2.0-2.5 mm, respectively.

To provide a basis for comparison to conventionally-fabricated/wrought or annealed material, half of the as-built SLM and DED tensile specimens were subjected to a heat treatment to eliminate

the distinctive AM microstructures. These specimens were heat-treated at 1000 °C for 1 hr under flowing Ar gas, followed by a water quench. This process reduced dislocation density, allowed diffusion of dendritic segregation patterns, and changed the grain structure of components to create microstructures more similar to wrought or annealed conventional components [38], while maintaining the bulk chemical compositions. The heat-treated specimens were mechanically ground to 600 grit sandpaper finish on front and back sides to remove the oxide layer that developed during heat treatment. Then one side was mechanically polished with diamond suspensions and a final 0.05 μm alumina suspension to a surface finish sufficient for electron backscatter diffraction (EBSD) mapping. The as-built specimens were mechanically polished in the same way prior to hydrogen charging and testing to achieve the same surface as the heat-treated specimens.

2.2 Materials and starting microstructures

SLM and DED methods produced materials with similar chemical composition, but different microstructures. Chemical compositional analysis was performed on the as-built SLM and DED parts after printing by Luvak Inc., utilizing combustion infrared detection, inert gas fusion, vacuum hot extraction, and direct current plasma emission spectroscopy methods. The compositions are listed in Table 1. These compositions satisfy the requirement by ISO 15510:2014 standard for steel designation of X2CrNiMo18-14-3.

Table 1. Compositions in weight percent and Md_{30} temperature of as-built SLM and DED materials.

	Fe	Cr	Ni	Mo	Mn	Si	C	Cu	N	O	S	P	Md_{30}
SLM	Bal.	18.39	13.94	2.86	1.47	0.30	0.004	0.0022	0.065	0.043	0.004	0.017	-71
DED	Bal.	18.06	13.79	2.86	1.58	0.32	0.005	0.0095	0.072	0.037	0.004	0.008	-70

Md_{30} represents the temperature at which 30% true tensile strain induces a transformation of 50% of the austenite into martensite and indicates the stability of austenite phase. This value was calculated using the following relationship:

$$Md_{30} = 413 - 462(C + N) - 9.5Ni - 13.7Cr - 8.1Mn - 18.5Mo - 9.2Si \quad (1)$$

where the composition for each element is given in weight percent and Md_{30} is given in degrees Celsius [42, 43]. The compositions and Md_{30} temperatures were similar for parts produced with both AM methods, with Md_{30} temperatures around -70 °C.

The microstructural differences between SLM and DED components have been characterized and reported in detail by Rankouhi et al. [38] and Bertsch et al. [39]. Both materials in the as-built state exhibit dense dislocation structures with segregation to interdendritic regions. The primary differences are in scale and density of various features.

In as-built SLM SS 316L, the dendritic structures overlap with dislocation cells with diameter approximately 470 nm, such that the microstructure is dominated by dislocation cells elongated on {001}-type crystallographic planes with segregation of primarily Cr.

In as-built DED SS 316L, dislocation cells with diameter approximately 370 nm are observed, but these are equiaxed, and while dendrites overlap with some of the dislocation walls, primary dendrite arm spacing (PDAS) is approximately 1.5-2.0 μm. This leads to a dual cell structure in as-built DED material that is characterized by large cells with segregation to the walls

superimposed on a background of small dislocation cells with uniform composition. Heat treatment of SLM material reduced the dislocation density, but left a defined dislocation structure, while heat treatment of DED material created a well-annealed microstructure. Key microstructural features of the materials are summarized in Table 2 (adapted from [38]).

Table 2. Length scales of key microstructural features in as-built and heat-treated AM materials (adapted from [38]).

		Equiaxed dislocation cell size (nm)	PDAS/ Dendritic dislocation wall spacing (nm)	Dislocation density (m ⁻²)	Precipitate diameter (nm)	Precipitate density (m ⁻³)	Grain size (μm)
SLM	As-built	-	470	4x10 ¹⁴ [39]	15	4.0x10 ²⁰	20
	Heat-treated	-	-	9x10 ¹³ [27]	40	0.3x10 ²⁰	16
DED	As-built	370	1500-2000	1x10 ¹⁴ [39]	120	0.8x10 ¹⁸	80
	Heat-treated	-	-	3.3x10 ¹³	200	1.4x10 ¹⁸	140

The degree of segregation within dendrites was quantified using energy dispersive spectroscopy (EDS) for each alloy, as outlined in [39]. EDS across dendrites indicated little fluctuation of Ni content, between approximately 12.5-14.0 weight% Ni, which occurred primarily within the noise range of the EDS detector. This was found to be true for both SLM and DED materials. On the other hand, clear Fe depletion (61-67 weight% Fe) and Cr segregation (16-20 weight% Cr) were found across dendrites. Elements such as C and N were not measured due to the limits of accuracy of the EDS detector, while other elements such as O, Si, Mn, and Mo exhibited minimal segregation across dendrites (in other words, within the signal to noise fluctuations) similarly to Ni. Precipitates were found to be enriched in O, Si, and Mn in both SLM and DED materials [38, 39].

For more details on the methods used to evaluate microstructural feature dimensions, the reader is directed to Rankouhi et al. [38] and Bertsch et al. [39]. Dislocation densities for as-built SLM and DED materials were calculated using the method reported in Bertsch et al. [39]. Dislocation density for SLM heat-treated material was estimated from Bronkhorst et al. [27], and density for DED heat-treated material was calculated as detailed in Supplementary Material (Supplemental Fig. 1).

Both SLM and DED parts were found to produce nominally fully-dense parts, without substantial differences in porosity, as reported previously [38, 44, 45]. Additionally, SEM imaging, fractography, and TEM imaging revealed similar low porosity/nominally full density in all specimens used in this study. SLM and DED parts were also not found to contain δ-ferrite, which is sometimes reported in AM SS 316L.

2.3 Microstructural analysis

Prior to microscopic analysis with EBSD, the mechanical damage layer of the tensile specimens that was accompanied by polishing was removed by electropolishing in a 0.05 M oxalic acid solution at 6 V for 1-2 min. Specimens were mapped via EBSD before and after tensile testing to analyze the grain morphology and deformation twinning behavior. EBSD mapping was performed in an FEI Helios G4 plasma focused ion beam (PFIB) CXe with an Elstar™ scanning electron microscope (SEM) column equipped with an Hikari camera operated at 30 kV

accelerating voltage. EBSD maps ranged from 1 to 2 mm² in size with step size from 0.7 to 2.0 μm.

Deformation microstructures were interrogated using scanning/transmission electron microscopy (S/TEM) analysis of thin foils. 3 mm disks were prepared for TEM analysis from rectangular bars that were deformed in tension, with tests interrupted at 15% elongation, by grinding down to approximately 200 μm thickness, punching out disks using a standard manual punch, and electropolishing disks to electron transparency. Electropolishing of TEM disks was performed in a Struers Tenupol twin-jet polisher using standard A2 solution at approximately 20 °C and 11-13 V for 15 min, followed by dipping in isopropanol and ethanol washes. Further, microstructures adjacent to or immediately beneath fracture surfaces were extracted for TEM analysis using FIB machining in the FEI Helios PFIB and a Zeiss Auriga model Ga FIB. A protective Pt layer was applied during the FIB machining process to preserve surface topography created by deformation on free surfaces or by failure on fracture surfaces; the Pt layer was edited out of some images for clarity in the present paper.

S/TEM analysis was performed in an FEI Tecnai TF-30 S/TEM operated at 300 kV and in an FEI Titan 80-200 aberration-corrected TEM operated at 200 kV. Bright field (BF) imaging was performed using the diffraction contrast STEM technique with a [011] zone-axis beam direction unless otherwise noted.

Orientation mapping of the foils was performed using transmission EBSD (t-EBSD) in the Helios PFIB, with step sizes approximately 40 nm and operating voltage 25-30 kV. Orientation analysis was performed utilizing the MTEX software package [46] for MATLAB.

2.4 Hydrogen charging and slow strain rate tensile testing

Some specimens were charged with hydrogen (after preparation of surfaces) in a high-pressure H₂ gas autoclave at 120 MPa and 280 °C for 400 h. This charging condition was chosen to homogeneously distribute hydrogen through the thickness of specimens prior to testing. All hydrogen-precharged specimens were stored in a refrigerator at 4 °C before SSRT tests to minimize egress of hydrogen. However, egress of hydrogen was not expected over the course of testing (up to 24 hours), setup, or shipping to the facilities for analysis (up to 5 days), due to the slow rate of diffusion of hydrogen in SS 316L [10, 47, 48].

Tensile specimens were subjected to SSRT testing in an MTS[®] Sintech load frame with a 50 kN load cell and 2.20 mV/V sensitivity. Tests were either interrupted at a prescribed intermediate strain or were performed to failure under constant-displacement testing. For interrupted tests, as-built and heat-treated SLM and DED samples were deformed to 15% elongation at a strain rate of 10⁻⁵ s⁻¹. 15% was within the range of uniform elongation region for all the tests. The interrupted tests allowed for evaluation of the influence of hydrogen on microstructural development prior to necking and failure. An MTS model 634-12F-24 knife-edge extensometer with custom-printed attachments to accommodate the small sample geometry was used to measure elongation of the interrupted samples.

For ruptured tests, as-built and heat-treated SLM and DED samples were tested to failure at an initial strain rate of 10⁻⁵ s⁻¹. For the specimens tested to failure, no extensometer was used to avoid crack initiation at the extensometer knife edge since hydrogen-charged materials can be highly susceptible to the influence of stress concentration, particularly with respect to the formation of a neck and failure. Stress-strain data reported for failed specimens was calculated from raw load-displacement data with a correction applied to the elastic regime based on calibrations from interrupted tests.

3. Results

3.1 Hydrogen content

Gas chromatograph thermal desorption analysis (GC-TDA) was performed after straining of both uncharged and hydrogen-charged materials to assess the retained hydrogen content. The results are shown in Fig. 1 and summarized in Table 3. Circle symbols indicate SLM material, squares show DED, while black symbols indicate as-built material and gray symbols correspond to heat-treated. Open symbols correspond to uncharged, while filled symbols indicate hydrogen-charged material; the uncharged material curves all overlap near the bottom of Fig. 1 due to their low hydrogen desorption rate.

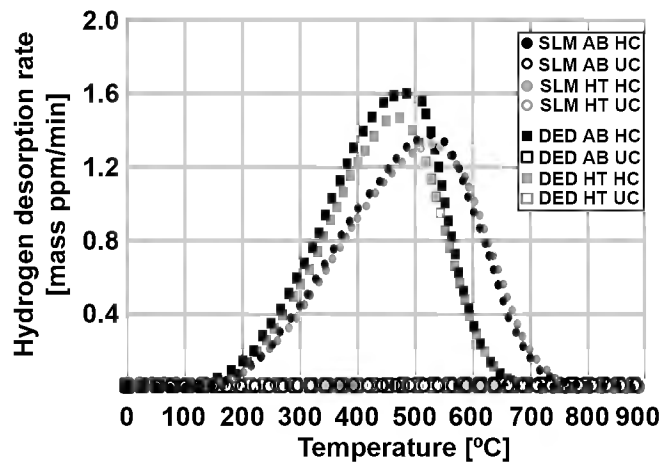


Figure 1. Thermal desorption analysis of uncharged (open symbols) and hydrogen-charged (filled symbols) parts, both SLM (circles) and DED (squares). As-built (AB) parts shown in black, heat-treated (HT) shown in gray.

Hydrogen-charged specimens contained between 107.8 and 121.2 mass ppm of peak 1 hydrogen content as catalogued in Table 3; the first peak that appears in a TDA spectrum is defined as peak 1 hydrogen in this study. No significant difference was found in hydrogen content between hydrogen-charged SLM and DED materials or between as-built and heat-treated states, although heat-treated materials contained slightly less hydrogen content than their as-built counterparts. DED specimens exhibited a lower desorption rate peak temperature than SLM specimens, at 463-480 and 522 °C, respectively. This difference in desorption rate peak temperature can be ascribed to the difference in as-built sample thickness; DED specimens were thinner than SLM specimens due to build differences, 2.0-2.5 mm compared to 3.0-3.5 mm, respectively. The uncharged specimens were found to contain between 0.1 and 1.0 mass ppm of hydrogen.

Table 3. Peak 1 hydrogen content and desorption rate peak temperature measured by thermal desorption analysis. UC and HC denote uncharged and hydrogen-charged, respectively.

	SLM				DED			
	As-built		Heat-treated		As-built		Heat-treated	
	UC	HC	UC	HC	UC	HC	UC	HC
Peak 1 hydrogen content (mass ppm; at. ppm)	0.7; 40	120.7; 6735	0.1; 8	117.5; 6559	1.0; 58	121.2; 6762	0.4; 24	107.8; 6017
Desorption rate peak temp. (°C)	-	522	-	522	-	480	-	463

3.2 Mechanical response

Mechanical properties were modified during heat treatment and due to the presence of hydrogen as shown in the engineering stress-strain curves in Fig. 2. Mechanical properties for the representative samples shown in Fig. 2 are summarized in Table 4.

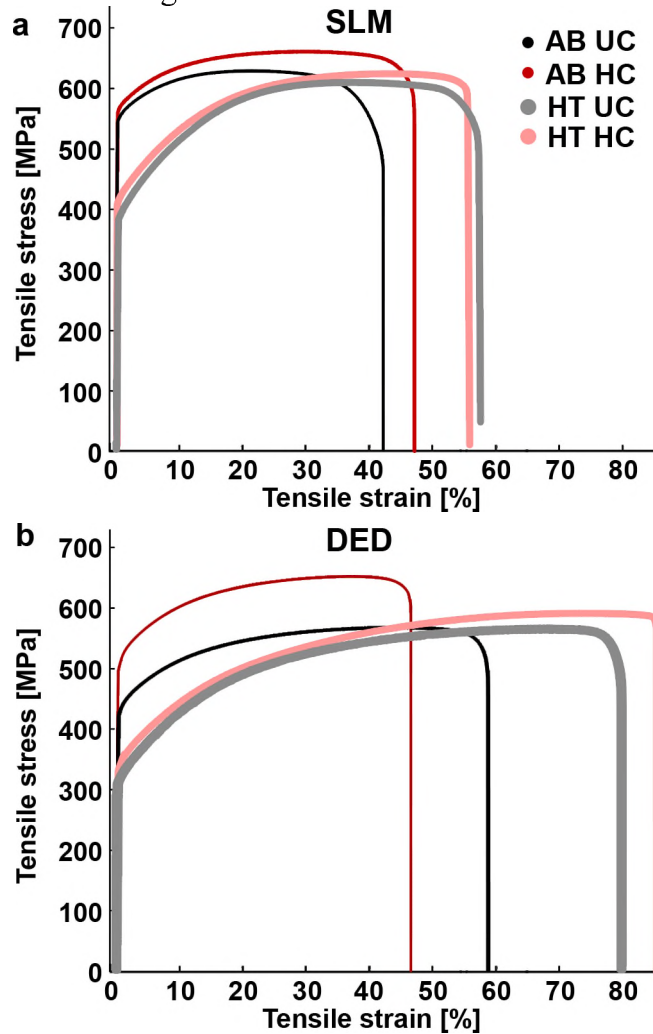


Figure 2. Engineering stress-strain curves for selected specimens of a. SLM and b. DED materials. Thin curves represent as-built materials (black for uncharged, red for hydrogen-charged), thicker curves represent heat-treated materials (gray for uncharged, pink for hydrogen-charged), for both a and b. Color online.

In Fig. 2, one representative sample curve was selected to display for each material, although multiple specimens were tested; additional information regarding the number and selection of samples can be found in Supplementary Material. As-built SLM material yielded around 548 MPa, while as-built DED material yielded around 429 MPa in the uncharged state. For both alloys in the uncharged state, heat treatment reduced the yield strength by approximately 30% and increased the strain-to-failure.

The presence of hydrogen increased the yield strength for all materials, most substantially for as-built DED material. For as-built SLM material, the yield strength was slightly increased in the presence of hydrogen, although the effect was small showing some variability in material response. The ultimate tensile strength was enhanced in the presence of hydrogen for all materials.

Most importantly, the presence of hydrogen did not significantly affect the macroscopic ductility of any of the specimens except for the as-built DED material, in which the elongation at failure was reduced by approximately 12.2%. The relative reduction in area (RRA), or ratio of the reduction in area in the presence of hydrogen divided by that in the absence of hydrogen, was also smallest in as-built DED material at 75% RRA, compared to 83-87% in other materials. These RRAs are slightly lower than previously reported for conventional SS 316L with similar Ni content [19], although experimental conditions such as specimen configuration, hydrogen charging and test temperature may be a factor. Since the largest differences between the materials in the current study were not compositional but microstructural, this suggests that the microstructures influenced the HE susceptibility. As can be seen in Table 4, the effect of hydrogen on mechanical response is more clearly found in RA or RRA than elongation. This suggests that the presence of hydrogen has a more significant influence on necking than on uniform deformation at the macroscopic level. Average properties and standard deviations are shown in Supplemental Table 1.

Table 4. Representative mechanical properties measured in uncharged (UC) and hydrogen-charged (HC) specimens.

			Yield strength (MPa)	Ultimate tensile strength (MPa)	Elongation at break (%)	Reduction in area (%)	Relative reduction in area (%) (RA_{HC}/RA_{UC}) \times 100
SLM	As-built	UC	548	628	42.2	72	83
		HC	564	660	47.1	60	
		Δ	16	32	4.9	-12	
	Heat-treated	UC	388	611	57.5	67	87
		HC	414	626	55.7	59	
		Δ	26	15	-1.8	-8	
DED	As-built	UC	429	567	58.8	76	75
		HC	505	651	46.5	57	
		Δ	76	84	-12.2	-19	
	Heat-treated	UC	316	566	79.7	69	84
		HC	339	592	85.3	58	
		Δ	23	26	5.6	-11	

3.3 Fracture surfaces

3.3.1 Fractography

Fracture surfaces of all ruptured specimens consisted of dimples consistent with failure by ductile microvoid coalescence irrespective of the presence of hydrogen, as shown in Fig. 3.

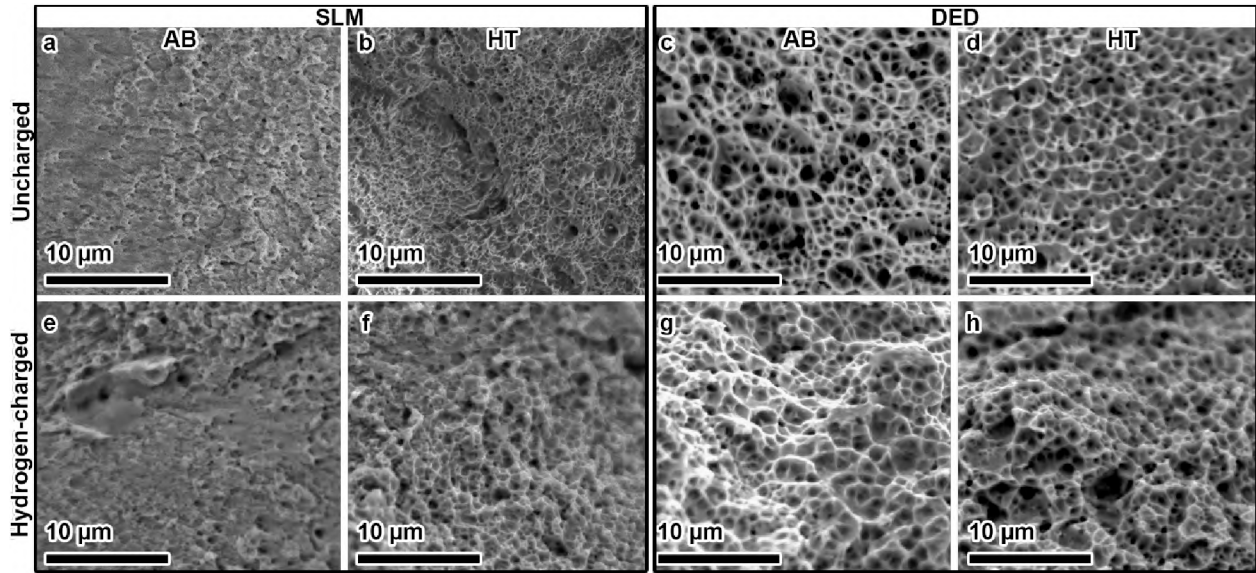


Figure 3. SEM fractographs of dimples on the fracture surfaces of a, e. SLM as-built, b, f. SLM heat-treated, c, g. DED as-built, and d, h. DED heat-treated materials. a-d (top row) uncharged, e-h (bottom row) hydrogen-charged.

Fracture surfaces were not affected qualitatively by the presence of hydrogen, as shown in Fig. 3; compare uncharged (top row) to hydrogen-charged (bottom row). This was confirmed by quantification of dimple size, summarized in Table 5. Dimples were smallest in SLM material, and nearly twice as large in DED specimens. The enhancement of dimple diameter in DED material compared to SLM is considered to reflect the lower precipitate density in DED material; lower density allows dimples to grow larger [38]. However, the presence of hydrogen had no significant effect on the average dimple size in any material, with variations falling well within standard deviation. In addition, precipitates were observed in the interior of many of the dimples in all materials.

Table 5. Average dimple diameter (nm) measured from SEM fractographs. UC and HC denote uncharged and hydrogen-charged, respectively. Average values are followed by one standard deviations.

SLM				DED			
As-built		Heat-treated		As-built		Heat-treated	
UC	HC	UC	HC	UC	HC	UC	HC
365 +/- 151	362 +/- 113	389 +/- 192	323 +/- 145	652 +/- 251	683 +/- 202	686 +/- 328	669 +/- 248

There was no evidence of flat or elongated dimples, or of tears characteristic of “quasi-cleavage” along deformation-induced martensite on the hydrogen-induced fracture surfaces, indicating that there was no change in failure mode in the presence of hydrogen [49]. To confirm the failure mechanisms, FIB machining was used to extract material directly beneath the fracture surface.

3.3.2 Voids and fracture paths

To analyze void formation near the fracture surface, S/TEM analysis was performed on lamellae extracted directly from fracture surfaces. Images of microstructures directly beneath fracture surfaces are presented in Fig. 4.

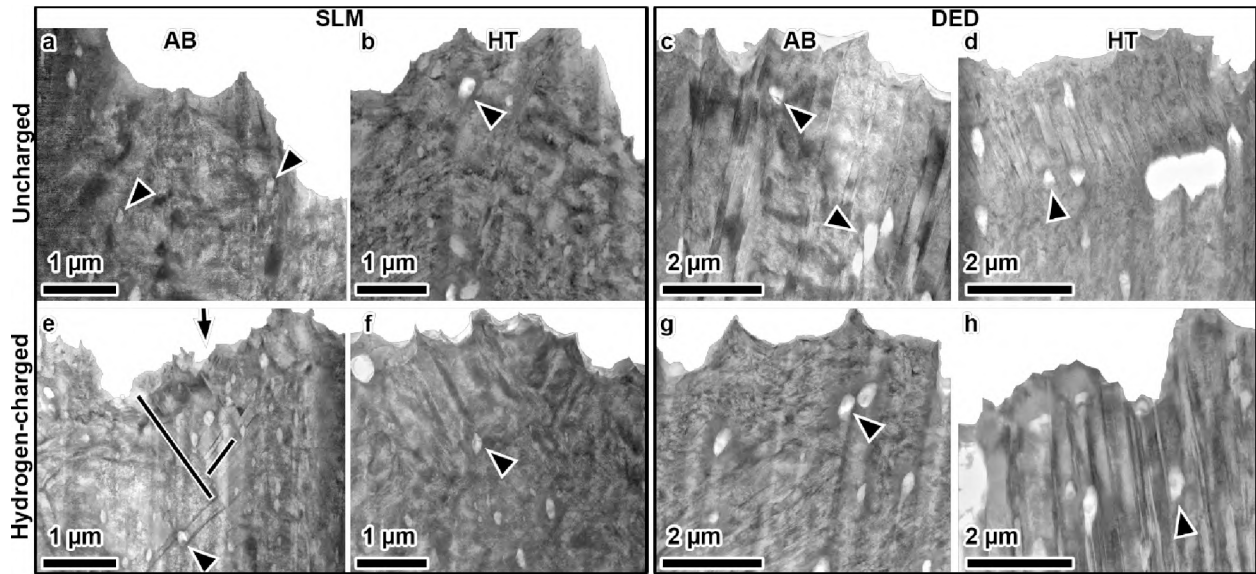


Figure 4. Bright-field STEM micrographs of microstructures underneath the fracture surfaces in a, e. SLM as-built, b, f. SLM heat-treated, c, g. DED as-built, and d, h. DED heat-treated materials. a-d (top row) uncharged, e-h (bottom row) hydrogen-charged. Arrowheads indicate voids. In e., solid black lines highlight twins and an arrow highlights a step on the fracture surface. Fracture surfaces shown at the top of each image; tensile axis is vertical.

In Fig. 4, the preserved fracture surfaces are shown at the top of each image, and the tensile axis is vertical. In as-built SLM material, fracture surfaces appeared to follow the subsurface deformation structures more closely in the presence of hydrogen. For example, in hydrogen-charged as-built SLM material, Fig. 4e, the step on the fracture surface indicated by the arrow corresponded to the directions of subsurface deformation twins, indicated by the solid black lines. In Fig. 4a, representing uncharged as-built SLM material, the fracture surface was rougher and could not be correlated to deformation bands or twins beneath the surface. This agrees with observations in the literature that found the fracture pathway in the presence of hydrogen can be influenced by twins [50, 51].

Similar observations were made in the heat-treated SLM material, where the microstructure was more closely correlated with steps on the fracture surface in the presence of hydrogen, as shown in Fig. 4f, than in the absence of hydrogen, Fig. 4b. Direct correlations between microstructure and surface steps was not observed in either as-built or heat-treated DED materials, with or without the presence of hydrogen, as shown in Fig. 4c, d, g, and h.

Voids were observed in all specimens beneath the fracture surfaces, with an increase in void density as the fracture surface is approached. Voids were observed distributed throughout the microstructure; examples are indicated by arrowheads in Fig. 4. This suggests that voids had nucleated throughout the material such as at grain boundaries, martensite interfaces, slip-band intersections, and precipitates.

Voids appeared qualitatively more numerous in the hydrogen-charged SLM material than in uncharged, e.g. compare Fig. 4a and e or Fig. 4 b and f. To quantify this, voids in bright-field STEM images were traced from the fracture surface to 20-30 μm deep in the material in each specimen. Void area was defined as inclusive of any precipitates observed within the void. This

analysis was limited to visible voids, which in the absence of high-resolution imaging included voids approximately 10 nm in diameter or greater. Consequently, nanovoid or vacancy populations were excluded from this analysis.

To calculate the number density of voids per unit volume, specimen thicknesses were estimated from edge-on SEM imaging of FIB-machined thin foils. The percentage area occupied by voids for material within the first 25 μm of the fracture surfaces, average void diameter, and number density of voids for all samples are shown in Table 6. The image area occupied by voids increased in the presence of hydrogen for every material. Void diameters and number densities are further compared in Fig. 5.

Table 6. Void sizes and distributions beneath the fracture surfaces for all samples. UC and HC denote uncharged and hydrogen-charged, respectively. Average values are followed by one standard deviations in void diameter.

	SLM				DED			
	As-built		Heat-treated		As-built		Heat-treated	
	UC	HC	UC	HC	UC	HC	UC	HC
Percent area occupied (%)	0.38	0.44	0.76	0.78	0.76	0.92	1.14	1.36
Average void diameter (nm)	150 +/- 70	130 +/- 40	180 +/- 70	150 +/- 50	210 +/- 80	240 +/- 80	260 +/- 100	320 +/- 130
Number density (10^{17} m^{-3})	8.7	14.5	12.4	20.4	9.6	9.2	9.5	9.7

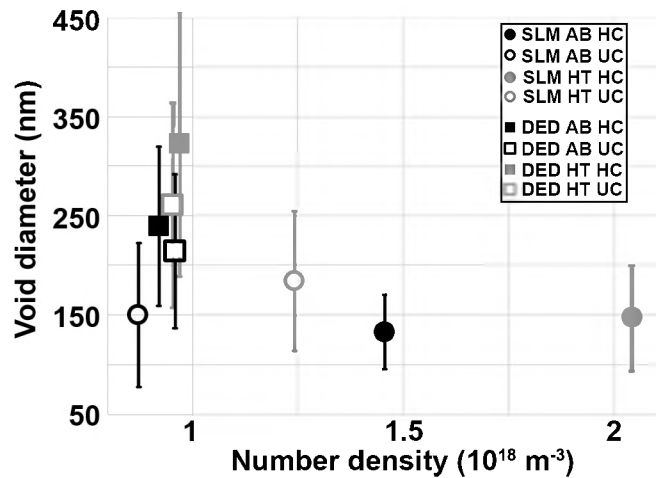


Figure 5. Average void diameter and number density for uncharged (open symbols) and hydrogen-charged (filled symbols) materials. SLM material indicated by circles, DED indicated by squares. As-built materials shown in black, heat-treated materials shown in gray.

In Fig. 5, open symbols represent uncharged material, filled show hydrogen-charged, circles indicate SLM and squares mark DED. Black markers represent as-built material and gray represent heat-treated. Several trends emerged from the void distribution data. First, in SLM materials, the void diameter decreased in the presence of hydrogen while the density increased. Conversely, in DED materials, void diameter increased in the presence of hydrogen. Little change to the density of voids due to the presence of hydrogen was found in DED materials.

3.4 Microstructural evolution

Since the starting compositions were similar in all materials, the different mechanical responses in the presence of hydrogen were hypothesized to be linked to differences in microstructural evolution throughout deformation. To investigate this, TEM microstructural analysis was performed at different stages of deformation, starting from 15% strain and going through necking and underneath fracture surfaces. The primary material of interest was the DED as-built material since it showed the most deleterious effect of hydrogen at the macroscopic level. The influence of hydrogen on microstructural evolution of the SLM as-built material is presented as well for comparison. Observations made in heat-treated materials were less detailed and are presented in Supplementary Material.

3.4.1 Microstructures at intermediate strain

Early microstructural development was evaluated in specimens interrupted at the same bulk elongation of 15%. This allowed for analysis of the influence of hydrogen on deformation prior to necking and failure. Strain of 15% was within the uniform elongation for all cases as seen in Fig. 2. Overall, the microstructures appeared very similar in the absence and presence of hydrogen, as shown in Fig. 6.

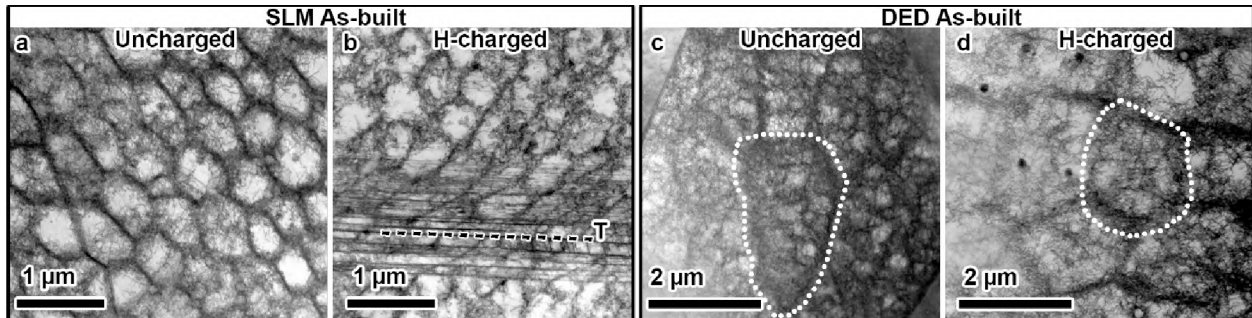


Figure 6. Bright-field STEM micrographs of dislocation structures at 15% elongation in a, b. SLM as-built, and c, d. DED as-built materials. Dashed line in b. parallel to deformation twins, dotted lines in c. and d. indicate dislocation cell walls with dendritic segregation profiles.

In SLM as-built material, the initial elongated dislocation cell structure remained apparent at 15% strain in both uncharged and hydrogen-charged alloys, Fig. 6a and b, respectively. The cell diameter remained approximately 470 nm average diameter, indicating that refinement was not initiated. In FCC alloys that typically form dislocation cells during deformation, cells subdivide and average cell size decreases with increasing deformation and dislocation density [52, 53]. Further, the presence of hydrogen has been shown to reduce the size of dislocation cells and accelerate the microstructural evolution at the same macroscopic strain level [54, 55]. The similarity of initial and 15%-deformed SLM as-built material, in both the uncharged and hydrogen-charged states, illustrates a departure from the response of conventional FCC alloys.

Deformation twinning had initiated in both uncharged and hydrogen-charged SLM as-built alloys, and twins were observed to shear and distort the cell structures, as indicated parallel to the dashed line labeled “T” in Fig. 6b. No significant difference was observed in the number, density, or thickness of twins between the uncharged and hydrogen-charged states.

In DED as-built materials, the initial structure remained evident at 15% strain irrespective of the presence of hydrogen, Fig. 6c and d. The dendritic dislocation walls were still visible in both the uncharged and hydrogen-charged specimens, for example as outlined by the dotted white lines in Fig. 6c and d. The smaller, equiaxed cells had begun to decrease in size, shrinking from their initial size of approximately 370 nm to an average diameter around approximately 150 nm in both

uncharged and hydrogen-charged materials. The similar cell size in the absence and presence of hydrogen indicates that, despite the effect of hydrogen to influence macroscopic plasticity at rupture, the plastic evolution up to 15% strain was similar. Deformation twinning had initiated in many grains in both the uncharged and hydrogen-charged specimens at 15% strain, but no substantial qualitative or quantitative difference was observed in the magnitude of twinning.

As compared to the as-built samples, the 15% elongation microstructure in heat-treated SLM material showed little change in the presence of hydrogen, whereas slip planarity was enhanced in the presence of hydrogen in heat-treated DED material, Supplemental Fig. 2. However, tk

3.4.2 Microstructure in the necked region

The continuing microstructural evolution in as-built materials was characterized by interrogating deformation structures in failed samples approximately 150-250 μm away from the fracture surfaces, within the necked region. This allowed for analysis of the microstructural development up to the onset of microvoid formation, while avoiding the documented effect of void coalescence to disrupt preexisting microstructures [56]. The free surfaces from which the specimens were extracted from as-built materials are shown in Supplemental Figs. 3 and 4 for reference.

Strain-induced martensite was not observed in the necked region of any of the materials either in the absence or presence of hydrogen. This absence of strain-induced martensite transformation was expected given the low M_{d30} temperatures of the materials in this study, Table 1.

Microstructures in the necked regions of uncharged and hydrogen-charged as-built SLM materials are shown in Fig. 7; the tensile axis is approximately horizontal. A bright-field STEM micrograph of the uncharged material is shown in Fig. 7a, while t-EBSD misorientation mapping of the same region is presented in Fig. 7c. Several grains were captured, as outlined with thick black lines in Fig. 7c. Each point is colorized according to the misorientation of that point with respect to a reference point. To account for the misorientations across grain boundaries, a different reference orientation was selected for each grain. Reference orientation points are indicated by the black dots with white outlines. Points with low confidence index were removed from the analysis and are shown in white. Deformation twin boundaries are indicated by the thick red lines, deformation boundaries with local misorientation 3° or greater are shown by the thin black lines.

In the uncharged SLM as-built material, deformation twins were a major part of the deformation microstructure at this level of strain. Twin bundles up to 500 nm thick in projection were observed, as shown in Fig. 7c. No comments will be made as to the true thickness of twin bundles and the volume of twins based on thin-foil measurements, since most twins could not be aligned edge-on with respect to the foil normal. Some grains contained twins in multiple directions as observed by STEM, although they were not clearly visible in the t-EBSD misorientation maps. For example, in the center grain in Fig. 7a, twins were observed in multiple directions parallel to the two crossed black lines, but only one set of these twins was clearly observed in the misorientation map of the center grain, as shown in Fig. 7c. Twins and deformation bands frequently exhibited local curvature, departing from planar configurations, as indicated near the arrow in Fig. 7a. Twins were most dense near grain boundaries.

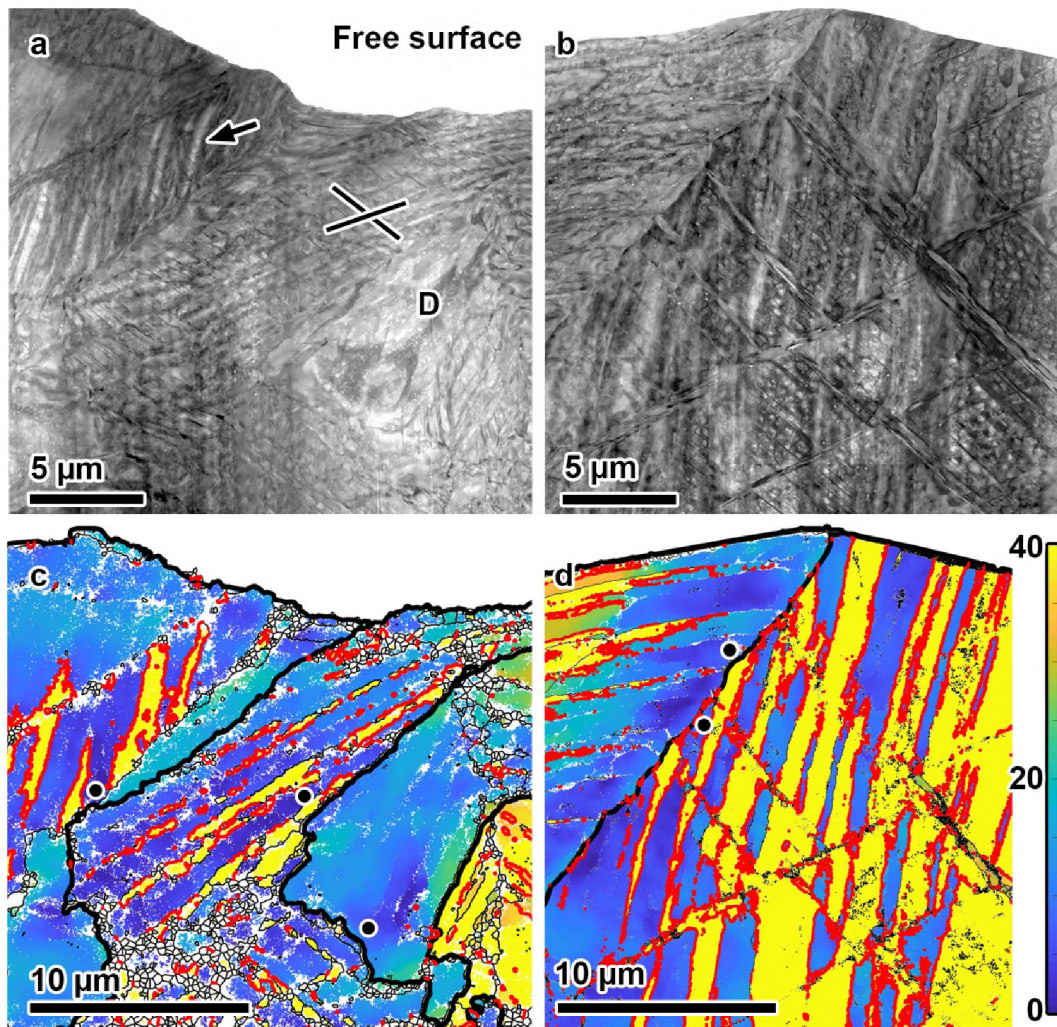


Figure 7. Bright-field STEM micrographs (top row) and misorientation maps (bottom row) in a, c. uncharged SLM as-built and b, d. hydrogen-charged SLM as-built materials. The free surface is at the top, and the tensile axis is approximately horizontal. In a., arrow indicates curved deformation bands, crossed lines are parallel to different twinning systems, and D represents a twin-free region with dislocation cells. In c, d., reference points indicated by black dots with white outlines; grain boundaries shown in thick black, deformation boundaries with local misorientation 3° or greater in thin black, twin boundaries in thick red. Color online.

Several regions in the uncharged as-built SLM material exhibited dislocation structures without local twinning, for example the region labeled “D” in Fig. 7a. In these regions, elongated dislocation cell structures were still a visible part of the microstructure, as shown in higher-resolution STEM images in Fig. 8a. Elongated and apparently-equiaxed cells were visible, although the elongated cells were found to be on ill-defined, various crystallographic planes, not the $\{001\}$ planes of the initial structures. The cell width had refined to approximately 200 nm or less, representing refinement from the initial state. Additionally, although dislocation walls were apparent, the cell interiors were less well-defined than was observed at lower strains, with considerable dislocation density between the walls, as shown in Fig. 8a.

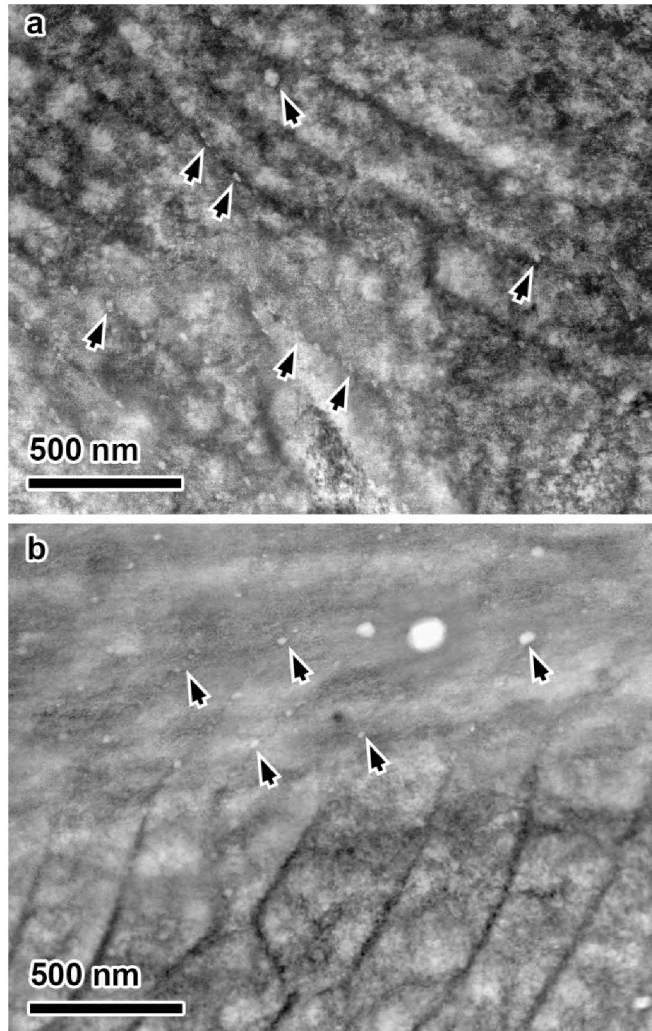


Figure 8. Bright-field STEM micrographs of dislocation structures up to 250 μm away from the fracture surfaces in a. uncharged SLM as-built and b. hydrogen-charged SLM as-built materials. Arrows indicate voids formed along dislocation walls.

Voids were observed along the elongated dislocation walls in the uncharged as-built SLM material, as indicated by the arrows in Fig. 8a. Voids were most frequently observed surrounding precipitates, although the level of strain and potential for removal of precipitates by the FIB milling process made it difficult to quantify the number of voids that formed around precipitates versus those that formed without precipitates, if any. At this strain level, voids were approximately 30 nm in diameter on average.

In the hydrogen-charged as-built SLM material, similar trends were observed. Deformation twins were observed on up to three different systems in a grain, as shown in Fig. 7b and d. Qualitatively, twins exhibited similar curvature as in uncharged as-built SLM material, particularly near grain boundaries, and similar overall area occupied. The extent of twinning is known to vary on a grain-by-grain basis, and can be affected by projection effects, so any quantitative comparisons would need to interrogate a larger number of grains than was analyzed here.

Notably, in the hydrogen-charged material, the orientation deviations as a function of distance from the grain boundaries appeared to be similar among neighboring grains, as shown in Fig. 7d. Elongated and equiaxed dislocation cell walls in hydrogen-charged material were qualitatively more defined than in uncharged material, as shown in Fig. 8b, although this effect was slight.

Voids followed approximately the same size distributions as in uncharged material, around 30 nm diameter, as shown in Fig. 8b, and no significant difference was observed in void placement.

The microstructure in the necked region in as-built DED materials similarly consisted of deformation twins and deformation bands, as shown in Figs. 9 and 10. Twins were observed on multiple systems in each grain, as indicated parallel to the straight black lines outlined in white in Fig. 9a and b, superimposed on a dense background of dislocations. Orientation deviations were similar in neighboring grains in uncharged as-built DED, similar to as-built SLM material, as shown in Fig. 9c.

Dislocation cells were not apparent at this strain level in uncharged DED as-built material, as shown in Fig. 10a. The microstructure consisted of twins and deformation bands, with some intermittent, disorganized dislocation tangles. Deformation bands exhibited curvature, for example as highlighted by the dashed lines in Fig. 10a, typical of interactions of multiple slip systems.

Voids in the uncharged as-built DED material were larger than those observed in SLM material, at around 200 nm average diameter, and were always observed surrounding precipitates, as indicated by the arrows in Fig. 10a. The precipitates appear as gray spherical or semi-spherical contrast inside the elongated lighter void regions. Unlike in SLM material, voids in uncharged as-built DED material were not observed to lie definitively along dislocation walls.

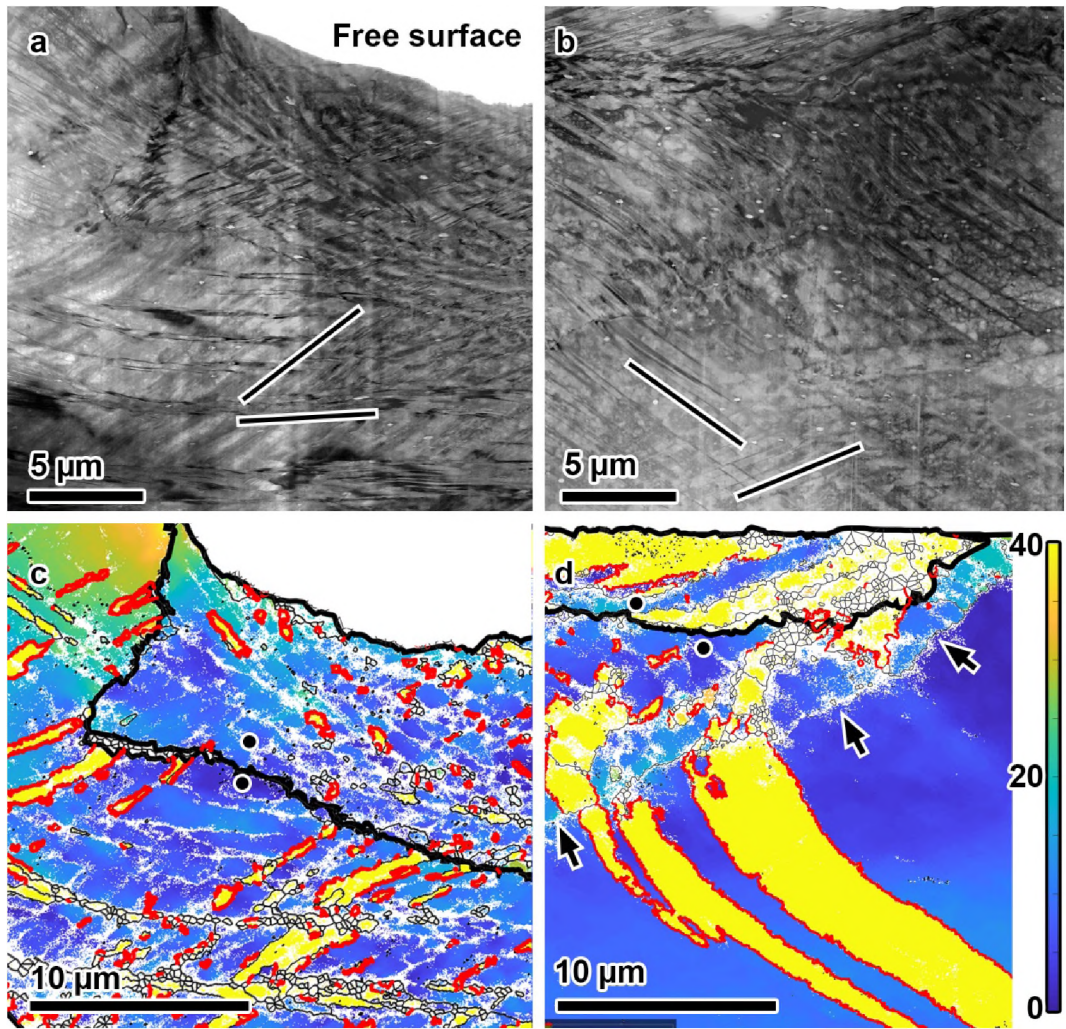


Figure 9. Bright-field STEM micrographs (top row) and t-EBSD misorientation maps (bottom row) in a, c. uncharged DED as-built and b, d. hydrogen-charged DED as-built materials. The free surface is at the top of images, and the tensile axis is approximately horizontal. In a, b., black lines with white outlines are parallel to different twinning systems. In c, d., reference points are indicated by black dots with white outlines; grain boundaries shown in thick black, twin boundaries in thick red. Color online.

In hydrogen-charged as-built DED material, fundamental differences were observed. Twins were present and often curved, but there were larger twin-free regions than in uncharged material, Fig. 9d. Defined dislocation cells still populated a significant portion of the microstructure; an example is outlined by the dotted white circle in Fig. 10b. The initial dual cell structure, with larger, dendritic dislocation cells superimposed on smaller, equiaxed cells, was no longer visible, yielding the cell structure shown in Fig. 10b. Deformation bands were still present, as indicated parallel to the dashed lines, but were sparse and did not dominate the microstructure as they did in uncharged as-built DED material. Orientation deviations were similar in hydrogen-charged and uncharged as-built DED material.

Voids in the hydrogen-charged material were approximately the same size as those observed in the uncharged material, with average diameter 200 nm, and were similarly observed surrounding precipitates. Examples of this are indicated by arrows in Fig. 10b.

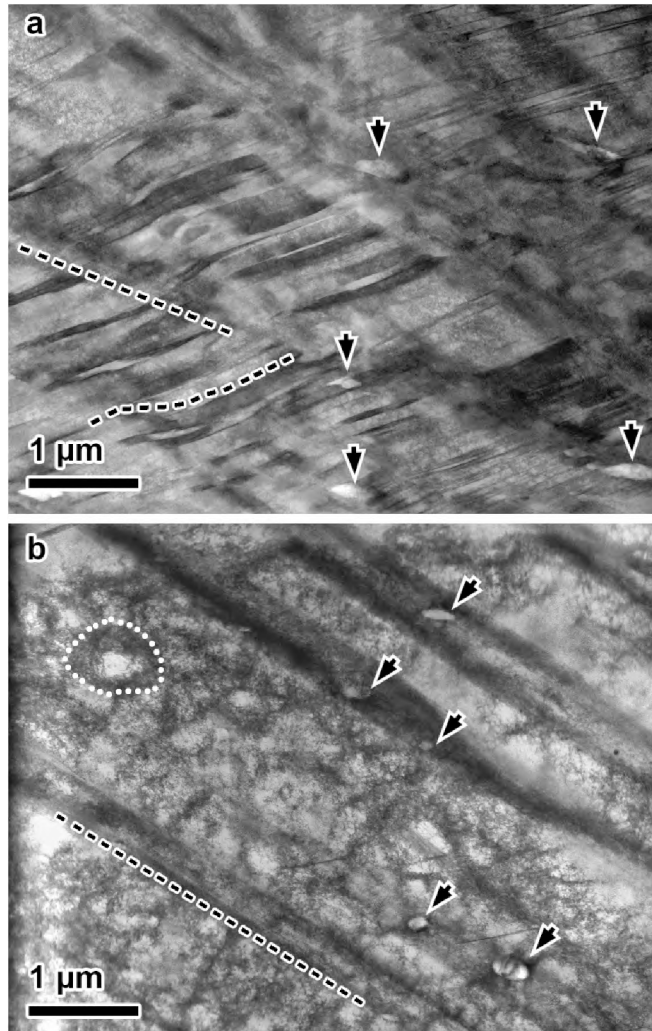


Figure 10. Bright-field STEM micrographs of dislocation structures up to 250 μm away from the fracture surfaces in a. uncharged DED as-built and b. hydrogen-charged DED as-built materials. Arrows indicate voids formed along dislocation walls. Dashed lines show deformation bands. A dotted white circle in b. indicates a well-defined dislocation cell.

In addition to S/TEM and t-EBSD analyses, EBSD orientation mapping was performed to analyze texture development in the necked region at the mesoscale. EBSD maps were taken from 0.5-1.0 mm from the fracture surfaces due to the difficulty indexing the heavily deformed regions closer to the fracture surfaces. EBSD maps and inverse pole figures showing the orientation distributions in as-built materials are shown in Fig. 11.

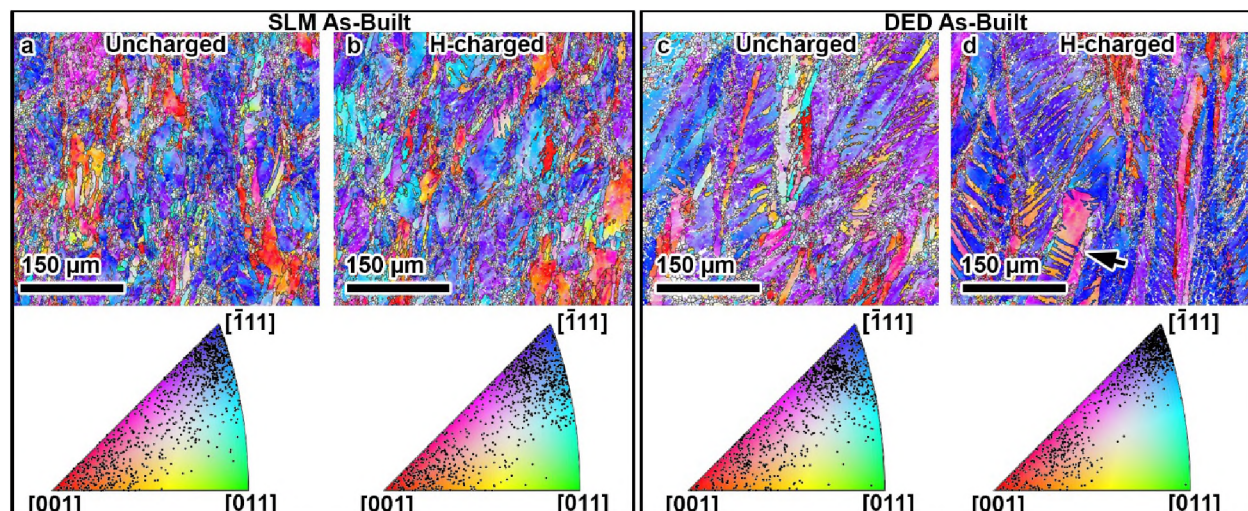


Figure 11. EBSD maps and stereographic triangle inverse pole figures representing texture in a. uncharged SLM as-built, b. hydrogen-charged SLM as-built, c. uncharged DED as-built, and d. hydrogen-charged DED as-built materials. Maps colorized according to the crystallographic orientation in the tensile direction (vertical in maps), and the color keys shown in the stereographic triangles. An arrow in d. indicates deformation twinning. Color online.

In the grain maps shown in Fig. 11a-d, the loading axis is vertical and the printing build direction is into the page. Grains were elongated in and oriented toward the loading direction in all materials compared to their initial grain structures. In all materials, preferential orientation distributions near $\langle 111 \rangle$ and $\langle 001 \rangle$ parallel to the tensile axis had developed, where the initial structures were essentially untextured in the loading direction, as reported in Rankouhi et al. [38].

In uncharged and hydrogen-charged as-built SLM materials, respectively shown in Fig. 11a and b, the orientation distributions and grain morphologies were essentially the same after deformation, which corresponds to the microstructural similarities observed. The size and area fraction of deformation twin bands were similar in uncharged and hydrogen-charged SLM as-built materials as well.

In uncharged DED as-built material, Fig. 11c, the orientation distributions observed were similar to those found in SLM material. In the hydrogen-charged DED material, the orientation distributions were more closely grouped towards the $\langle 001 \rangle$ - $\langle 111 \rangle$ edge of the stereographic triangle, particularly near the $\langle 111 \rangle$ corner, Fig. 11d. Since grains in FCC materials typically rotate towards $\langle 111 \rangle$ parallel to the loading axis during deformation, a greater $\langle 111 \rangle$ texture may be indicative of more advanced microstructural evolution. However, comparison of the microstructural states is not as straightforward as this in the as-built DED materials, given the differences in dislocation and deformation band structures observed in the absence and presence of hydrogen. Greater $\langle 111 \rangle$ texture evolution in the presence of hydrogen in DED materials would be counter to observations in FCC Ni that indicated less texture evolution in the presence of hydrogen [54].

Deformation twinning was observed in DED as-built material with and without hydrogen, for example visible as the bands indicated by the arrow in Fig. 11d. Little qualitative difference was observed in twinning patterns between uncharged and hydrogen-charged as-built DED materials, compare Fig. 11c and d. Strain-induced martensite was not detected in EBSD maps for any material.

3.4.3 Microstructure directly beneath fracture surfaces

The microstructures up to 25 μm beneath fracture surfaces were interrogated to analyze the influence of hydrogen on final failure patterns. Diffraction-contrast STEM imaging was combined with t-EBSD mapping to verify the presence of different features, particularly strain-induced martensite, deformation twinning, subgrain band formation, and orientation deviations. No substantial differences were observed in the presence of hydrogen in any materials; comparisons are shown in Supplemental material as Supplemental Figs. 5-8.

4. Discussion

4.1 Summary of microstructural differences and microstructural evolution

The most notable influences of hydrogen on the deformation response in the AM 316L alloys can be summarized as follows:

1. Mechanical response.
 - a. The presence of hydrogen increased yield strength in all materials.
 - b. All samples showed dimple morphology on the fracture surfaces both in the absence and presence of hydrogen.
 - c. The presence of hydrogen caused a clear reduction in elongation at failure only in as-built DED material, which showed the lowest relative reduction in area in the presence of hydrogen as well.
2. Microstructural evolution.
 - a. Dislocation cell structures were more prevalent and defined in the late stages of plasticity in hydrogen-charged as-built DED material than in uncharged.
 - b. Texture evolution was more evolved in the late stages of plasticity in hydrogen-charged as-built DED material than in uncharged.
3. Twinning.
 - a. Slightly more twinning was observed in the final stages of plastic deformation beneath the fracture surface in the presence of hydrogen in as-built DED material.
4. Void formation.
 - a. Voids appeared to initially nucleate along elongated dislocation walls in SLM materials.
 - b. The presence of hydrogen reduced average void size in SLM materials, but increased it in DED materials.
 - c. The presence of hydrogen increased void density in SLM materials, whereas it showed little difference for DED materials.
 - d. The average image area occupied by voids increased in the presence of hydrogen in all materials.

To more clearly link microstructural changes to tensile response, the influence of hydrogen on various microstructural features and ductility are tabulated in Table 7.

Table 7. Influence of hydrogen on different microstructural features and tensile properties. “-” indicates no significant difference, while N/A denotes that a feature was not evaluated.

		Elongation at break (%)	Relative reduction in area (%)	Dislocation structure			Mesoscale deformation patterns	Void size (sub-fracture surface)	Void density (sub-fracture surface)	Dimple structure
				15% strain	Necked region	Sub-fracture surface				
SLM	As-built	4.9	83	-	-	-	-	Reduced	Increased	-
	Heat-treated	-1.8	87	-	N/A	-	-	Reduced	Increased	-
DED	As-built	-12.2	75	-	More defined cells	-	Enhanced texture evolution	Increased	-	-
	Heat-treated	5.6	84	Enhanced planarity	N/A	-	-	Increased	-	-

In the following, the differences in response between the materials are analyzed and the relative influence of the different features of the initial microstructures is discussed. As shown in Table 7, the most significant loss of ductility was observed in as-built DED material, so particular focus is paid to differences between the as-built DED material and other materials. As-built DED material was the only material that exhibited more defined dislocation cells and slightly enhanced texture evolution. Other changes induced by hydrogen, such as enhanced planarity in heat-treated DED material or changes to void structure, did not appear to be linked to significant changes to tensile response. Thus, the interactions between hydrogen and dislocation structure/deformation patterns are highlighted as potential reasons for the heightened susceptibility of as-built DED material to HE. It will be shown that differences in the initial dislocation structures are likely to be correlated to the increased macroscopic influence of hydrogen, with possible minor influences of segregation patterns.

4.2 Influence of dislocation structures and deformation twinning

The effect of the initial and deformation-induced microstructure on the HE response of SS has been studied extensively, with many studies showing opposing effects. The effects are heavily dependent on the type of microstructural defects present. Strain-induced martensite formation, particularly α' , has been shown to influence the susceptibility of SS to HE [57-60], although the correlation has been shown not to be simple or direct [2, 12, 20, 21, 37]. In the current work, martensite was not detected in the initial or post mortem microstructure. It is possible some ϵ martensite was present but undetected immediately beneath the final fracture surfaces, due to the exceptionally high local strains obfuscating indexing. However, this is considered unlikely due to the absence of “quasi-cleavage” features on any fracture surfaces, as well as the low M_d30 temperatures. Further, any martensite phase was not detected in materials extracted adjacent to the fracture surfaces, indicating that it was not present in significant amounts prior to the final microvoid coalescence event. It was therefore concluded that strain-induced martensite formation was not a significant mechanism affecting the microstructural response in the current study.

In the absence of martensite, the influence of prestrain on susceptibility to HE has been reported to vary widely. Studies have shown a detrimental effect of prestrain [61], no significant effect of prestrain [12], or beneficial effect of increasing dislocation density [62]. Still other studies have indicated that susceptibility to HE initially increases with level of prestrain, then decreases at higher levels of prestrain, suggested to occur at a “critical” dislocation density for 316 type SS [20] as well as for α Fe [63]. In the current work, the heat-treated materials with low initial dislocation density appeared to be resistant to HE effects, as did as-built SLM material with the highest dislocation density. However, HE susceptibility was increased for as-built DED material with dislocation density on the same order of magnitude as the as-built SLM material. This indicates that, similar to the overall literature results, the influence of dislocation density on susceptibility is not direct. In fact, the TDA results, Fig. 1 and Table 3 show similarity of hydrogen content among tested materials irrespective of lower dislocation density of heat-treated materials. This suggests that the initial dislocation density does not have a substantial influence on the initial hydrogen concentration. Accordingly, it is suggested that the primary influence of the initial dislocation structure on susceptibility to HE is indirect and not related to an increase in overall initial hydrogen content.

Once hydrogen and dislocations begin to interact during deformation, they have several mutual influences. Hydrogen reduces stacking fault energy (SFE) and reduces the line energy of edge dislocations compared to screw dislocations, which reduces cross slip and enhances slip planarity [1, 64-66]. These effects have been linked to localization of slip and shear band formation [67-71], but the overall influence on the evolution of deformation and the onset of failure is less clear [2]. For example, SFE has been shown not to be directly correlated with susceptibility to HE [10], and the reduction in SFE has been estimated at only approximately 20% [72]. Recent studies have indicated that the slight reduction in SFE can indirectly drive a preference for ϵ martensite formation over deformation twinning, which then enhances α' martensite formation and embrittlement [73]. In the current study, neither localization, substantial shear banding, nor martensite formation were observed in any of the steels. Thus, it is considered unlikely that differences in SFE or slip planarity were the primary drivers for the differences in tensile response observed in the current study. This is further supported by the observation that slip planarity was enhanced in the presence of hydrogen in heat-treated DED material, but the tensile properties and failure were not negatively affected, as shown in Table 7.

Hydrogen can also be attracted to the stress fields surrounding dislocations, causing a decrease in inter-dislocation spacing and enhancing dislocation mobility [31], including in SS 316L [74]. Once hydrogen has accrued in the stress fields of mobile dislocations, it can also be transported through the lattice [75-77]. Hydrogen has been shown to accelerate the evolution of dislocation microstructures with strain by reducing the average dislocation cell size for a given level of strain in Ni and Fe [54, 55, 78]. This cell size reduction has been attributed to the effect of hydrogen to reduce the minimum spacing between dislocations, which dictates the minimum cell size, as well as enhances generation of dislocations [52, 55]. Hydrogen accumulated in the stress fields of these dislocation structure has been suggested to make reorganization less favorable during later stages of deformation, contributing to “locking-in” of the microstructure [54, 79].

The influence of hydrogen on cell size refinement has received less attention in materials like SS 316L that have additional deformation mechanisms such as twinning and martensite transformation. Twins accommodate deformation by different mechanisms than dislocations, and their nucleation and growth have been indicated to be mechanisms for local stress relief [80-82]. Twinning has been suggested to have different dynamic interactions with hydrogen than

dislocations [51, 83], and so may provide a means of deforming even when microstructures are influenced by the presence of hydrogen around dislocation stress fields. Thus, the interplay between hydrogen and deformation becomes more complex in these materials. Studies of compositionally complex alloys with FCC structure and deformation twinning modes have indicated that hydrogen stabilizes dislocation cell structures in the late stages of deformation, resulting in less twinning [84]. In studies of SS 316L after fatigue loading, the presence of hydrogen allowed for dislocation cells to persist to later stages of strain than in uncharged material by decreasing the minimum cell size attainable before initiating twinning [11, 85].

In the SS 316L materials in this study, while cell refinement was not substantially affected by the presence of hydrogen in any material, hydrogen enhanced the prevalence of well-defined dislocation cells in as-built DED material near the final fracture surface. As-built DED material also exhibited the most significant detrimental effect of hydrogen on the tensile properties, see Tables 4 and 7. This supports a correlation between the stabilization of dislocation cell structures (compared to twins and banded deformation structures) in the presence of hydrogen and a negative effect on failure in materials. In this case, it is then critical to understand why enhancement of dislocation cell structures were not observed in the other materials in this study.

The effect of hydrogen to refine and stabilize dislocation cell structures has most commonly been observed for materials in the well-annealed condition, with sparse initial dislocation density. However, as-built SLM, heat-treated SLM, and as-built DED materials all exhibited initial dislocation structures with different morphologies [38]. While the effects of prior cold work and initial dislocation density on the bulk response to hydrogen have been investigated in many studies, the influence of subtle differences in dislocation organization and morphology has received much less attention. For example, studies of high-rate-energy forged (HERF) samples [62, 86], which exhibit dislocation tangles without cell formation, indicated that HERF samples showed increased resistance to HE compared to annealed samples. This may indicate that hydrogen interactions with less-organized dislocation structures may be beneficial. While elongated, defined cells were present in as-built SLM material, their relatively large size could have created similar conditions to those in HERF materials, leading to less influence on embrittlement. This could also apply to heat-treated SLM material, which exhibited some elongated structures but even less organization and wider spacing, and are expected to have uniform composition due to the thermal treatment [87-89], similar to conventional wrought or annealed material. The smaller initial cell size in as-built DED material may have created conditions that reduced the ability of cells to re-organize in the presence of hydrogen.

Further, as-built DED material exhibited equiaxed cells compared to the elongated cells in SLM materials. The orientation of elongated SLM cells relative to the loading direction compared to the equiaxed structures observed in as-built DED material could also influence the exchange of dislocations, as evidenced by the differences in microstructural evolution as a function of strain level. Consequently, the orientation of initial dislocation structures could influence the exchange of hydrogen through the material.

It should be noted that the beneficial effect of loosely-organized dislocation structures was not always observed for HERF material [90]. Given this variation in reports of the effects of prior microstructures on HE of SS, conclusions regarding the influence of the organization of the prior dislocation structure on HE susceptibility with the available data remain speculative. This is particularly true for any conclusions regarding the effects of dislocation structures in conventional or annealed wrought material, given the differences between heat-treated specimens in the current study and true conventional wrought or annealed material, such as precipitate structures and

potential lingering porosity. However, based on the results of the current study, it can be surmised that the form of the initial dislocation structures, in addition to the dislocation density, may be influential in determining HE susceptibility in SS, which will warrant additional, systematic exploration.

4.3 Influence of mesoscale deformation patterns

At a larger length scale, the acceleration and “locking-in” of microstructures in the presence of hydrogen has been shown to affect orientation deviations. In the presence of hydrogen, orientation deviations have been shown to be higher and more localized in one grain than in the neighboring grain across a boundary, while orientation deviations tend to be similar across grain boundaries in the absence of hydrogen [54, 79, 91]. These effects of hydrogen were also suggested to reduce the ability of grains to rotate during deformation in Ni [54]. For FCC metals, grains tend to rotate towards $\{111\}$ orientations parallel to the tensile direction, resulting in an increase in $\{111\}$ texture after deformation [92]. Thus, reduced rotations of individual grains would decrease the development of $\{111\}$ texture, as has been observed for Ni. Conversely, as-built DED material in the current study saw an increased development of $\{111\}$ texture, as shown in Fig. 11, despite the apparent stabilization of dislocation cell structures, and orientation deviations were similar in all materials. The presence of deformation twinning may explain this observation.

In materials like 316L SS, deformation twinning may relieve some of the constraints imposed by the hydrogen-affected dislocation organization. The relief of constraints would allow for deformation to continue by a combination of twinning and dislocation slip where it would be constrained in non-twinning materials. This could allow for more enhanced texture to develop despite the effect of hydrogen to reduce reorganization of dislocation structures by cross-slip. The presence of twins has been observed to influence the texture evolution such that the texture present at the onset of twinning is refined [93, 94]. Thus, twins may not *directly* influence texture evolution, but instead primarily influence how deformation can proceed in the presence of hydrogen, which would *indirectly* influence the texture evolution. Further study is needed to elucidate the influence of twinning on texture and orientation deviations, particularly on larger areas including more grains.

4.4 Influence of segregation

Chemical segregation in the microstructure has been shown to influence the HE resistance of SS [19, 30], although this has primarily been linked to the influence of local composition on martensite transformation [19]. In welded SS, dendritic patterns appeared on fracture surfaces; this effect was enhanced by the presence of hydrogen [30]. This was suggested to indicate a correlation between failure and local compositional variations as well. In the current study, dendritic features were not observed on fracture surfaces, with dimples exhibiting dependence on precipitate size and distribution instead. Variations in Ni content were also low, even in the as-built materials with known dendrites, and Ni content was high enough that martensite formation was negligible. These results could be interpreted to indicate that the microsegregation along dendrites or cells in as-built materials did not play a significant role in the HE response.

However, the dendritic structure varied significantly between the as-built materials, particularly with respect to length scale. As shown in Table 2, dendrites were approximately 3-4 times as large in as-built DED material than in as-built SLM. While variations in Ni content were low, segregation of elements such as C and N were not measured by EDS. C, N, and other elements can significantly affect the SFE as well as hydrogen trapping and HE [95-98]. Reports have

indicated that the length scale of hydrogen transport, which could be expected to occur between cells in the initial structure, may affect the HE resistance as well [20].

If this effect occurs and is affected by dendritic segregation, then the smaller length scale of the as-built SLM dendrites could potentially limit hydrogen transport and its ability to affect the microstructural evolution. This effect would depend on the species and extent of segregation, and would have a complex interplay with the dislocation structure influence on hydrogen transport. Further study is needed to determine the explicit influence of microsegregation, including more detailed studies of the evolution of solute-rich regions through the later stages of strain.

4.5 Influence of precipitates

Phase interfaces can function as sinks for hydrogen [99-101], either trapping diffusible hydrogen [102] or acting as sites for crack initiation and propagation [30, 103] depending on the size and distribution. In the current study, TDA indicated that differences in precipitate size and distribution did not have a significant effect on overall hydrogen concentration, Fig. 1 and Table 3. This suggests that the precipitates did not initially capture a significant volume fraction of diffusible hydrogen in either SLM or DED materials.

To confirm differences in the trapping ability of precipitates in the SS 316L alloys in this study, analysis of the binding energies of hydrogen to the precipitates is required. Both as-built SLM and DED materials contained Si-rich oxides, while heat-treated SLM and DED materials contained Mn- and Cr-rich oxides [38, 44]. Chemical differences would be expected to influence the binding energy and trapping abilities of the oxides. However, even without this information, it can be concluded that precipitates were likely not influential to the overall hydrogen uptake. Possible reasons for this could include the majority of hydrogen remaining in the lattice instead of at oxide interfaces, or precipitates being generally too widely distributed in the low-diffusivity austenite matrix.

Precipitates are known to act as nucleation sites for ductile microvoids [104-108] during failure, for example as shown in SS welds in both the absence and presence of hydrogen [30]. While hydrogen has been observed to enhance strain-induced vacancy formation [4, 61, 109-111], this is considered unlikely to influence the growth of the substantially larger voids given the stresses that would be required [1]. In the current study, the distribution of dimple sizes followed similar trends to precipitate size in both the absence and presence of hydrogen, Tables 2 and 5. This suggests that the precipitates were a critical factor in determining the nucleation and growth of voids and also that any effect of hydrogen on the nucleation of voids around precipitates was minor.

This minor influence is supported by observations that despite the increase in void density in the presence of hydrogen in SLM materials, there was no significant influence of hydrogen on strain at failure in SLM materials. The increase in void area due to hydrogen was smaller in as-built DED materials, 0.16%, than in heat-treated DED materials, 0.22%, and yet the macroscopic influence of hydrogen was greater in as-built DED material. This suggests that any effect of hydrogen to increase void density or area was not influential in determining the conditions leading up to final macroscopic failure and bulk mechanical response in the materials in this study.

The lack of correlation between small differences in void nucleation due to hydrogen and bulk mechanical response due to the presence of hydrogen is in good agreement with results reported by San Marchi et al. [12]. In their study, even though the presence of hydrogen reduced the size of dimples on the fracture surfaces, indicating a possible effect of hydrogen on void nucleation, SS 316L materials showed generally similar elongation at failure and RRA in the absence and

presence of hydrogen. This further supports the concept that changes to vacancy or void formation are not directly related to obvious changes to failure.

Hence, it can be surmised that differences in the initial dislocation structures are likely to be correlated to the increased macroscopic influence of hydrogen, with possible minor influences of deformation twinning, segregation patterns and precipitates.

5. Conclusions

1. For SS 316L with approximately the same composition produced by different AM methods with different microstructures, the hydrogen response was different.
 - a. In SLM as-built, SLM heat-treated, and DED heat-treated materials, hydrogen did not cause significant embrittlement.
 - b. In DED as-built material, hydrogen caused a reduction in ductility and RRA.
2. Despite the higher yield strength in the SLM as-built material compared to the DED as-built material, SLM 316L maintains resistance to HE, while the DED process enhances susceptibility to HE. This suggests that differences in the initial microstructures are closely tied to the differences in response to hydrogen environment as shown in Table 7.
 - a. Void area was increased in the presence of hydrogen in all materials, but this was not linked to changes in failure or mechanical response.
 - b. In as-built SLM material, deformation microstructures were not affected by the presence of hydrogen. In as-built DED material, equiaxed dislocation cells were present at later stages of deformation and texture was more evolved in the presence of hydrogen.
 - c. Differences in the response to hydrogen are linked to differences in the initial microstructures, particularly the morphology and spacing of dislocation structures, which have received less attention historically. Deformation twinning, dendritic segregation, and precipitates are considered to have a less significant effect, although further detailed study on embrittlement in DED as-built specimens is needed to fully elucidate the mechanisms responsible for embrittlement.

The relationships outlined above serve as an initial framework for selecting and qualifying AM materials for use in hydrogen environments. The results suggest that SLM SS 316L may be a candidate for use in hydrogen environments due to its relatively high yield strength and resistance to the detrimental effects of hydrogen on mechanical response.

6. Acknowledgements

The electron microscopy was carried out using facilities and instrumentation that are partially supported by the NSF through the Materials Research Science and Engineering Center (DMR-1720415). The authors would like to acknowledge further support from the Department of Energy / National Nuclear Security Administration under Award Number DE-NA0003921, the NSF-DMREF through the grant DMR-1728933, and NSF through the grant CMMI-1561899. Authors would also like to thank the Grainger Institute for Engineering for seeding this research activity. The EOS M290 was supported with UW2020 WARF Discovery Institute funds. KMB gratefully acknowledges support from Lawrence Livermore National Laboratory; Lawrence Livermore National Laboratory is operated by Lawrence Livermore National Security, LLC, for the U.S.

Department of Energy, National Nuclear Security Administration under Contract DE-AC52-07NA27344. KMB is partially supported by the Laboratory Directed Research and Development (LDRD) program (20-SI-004) at Lawrence Livermore National Laboratory. AN gratefully acknowledges the support of the International Institute for Carbon Neutral Energy Research (WPI-I2CNER), sponsored by the World Premier International Research Center Initiative (WPI), MEXT, Japan.

Disclaimer: This report was prepared as an account of work sponsored by an agency of the United States Government. Neither the United States Government nor any agency thereof, nor any of their employees, makes any warranty, express or implied, or assumes any legal liability or responsibility for the accuracy, completeness, or usefulness of any information, apparatus, product, or process disclosed, or represents that its use would not infringe privately owned rights. Reference herein to any specific commercial product, process, or service by trade name, trademark, manufacturer, or otherwise does not necessarily constitute or imply its endorsement, recommendation, or favoring by the United States Government or any agency thereof. The views and opinions of authors expressed herein do not necessarily state or reflect those of the United States Government or any agency thereof.

7. Data Availability

The raw/processed data required to reproduce these findings cannot be shared at this time due to technical or time limitations.

8. References

- [1] I.M. Robertson, P. Sofronis, A. Nagao, M.L. Martin, S. Wang, D.W. Gross, et al., Hydrogen embrittlement understood, *Metall. Mater. Trans. B* 46(3) (2015) 1085-1103. <https://doi.org/10.1007/s11663-015-0325-y>.
- [2] M.L. Martin, M. Dadfarnia, A. Nagao, S. Wang, P. Sofronis, Enumeration of the hydrogen-enhanced localized plasticity mechanism for hydrogen embrittlement in structural materials, *Acta Mater.* 165 (2019) 734-750. <https://doi.org/10.1016/j.actamat.2018.12.014>.
- [3] M.B. Djukic, G.M. Bakic, V. Sijacki Zeravcic, A. Sedmak, B. Rajicic, The synergistic action and interplay of hydrogen embrittlement mechanisms in steels and iron: Localized plasticity and decohesion, *Engin. Frac. Mech.* 216 (2019) 106528. <https://doi.org/10.1016/j.engfracmech.2019.106528>.
- [4] M. Nagumo, K. Takai, The predominant role of strain-induced vacancies in hydrogen embrittlement of steels: Overview, *Acta Mater.* 165 (2019) 722-733. <https://doi.org/10.1016/j.actamat.2018.12.013>.
- [5] S. Lynch, Understanding mechanisms and kinetics of environmentally assisted cracking, *BHM Berg- und Hüttenmännische Monatshefte* 161(1) (2016) 3-18. www.doi.org/10.1007/s00501-016-0448-8.
- [6] W. Gerberich, Modeling hydrogen induced damage mechanisms in metals, in: R.P. Gangloff, B.P. Somerday (Eds.), *Gaseous Hydrogen Embrittlement of Materials in Energy Technologies*, Woodhead Publishing, 2012, pp. 209-246. <http://doi.org/10.1533/9780857095374.2.209>.
- [7] M. Koyama, E. Akiyama, Y.-K. Lee, D. Raabe, K. Tsuzaki, Overview of hydrogen embrittlement in high-Mn steels, *Int. J. Hydrogen Energy* 42(17) (2017) 12706-12723. <https://doi.org/10.1016/j.ijhydene.2017.02.214>.
- [8] M.L. Martin, J.A. Fenske, G.S. Liu, P. Sofronis, I.M. Robertson, On the formation and nature of quasi-cleavage fracture surfaces in hydrogen embrittled steels, *Acta Mater.* 59(4) (2011) 1601-1606. <http://doi.org/10.1016/j.actamat.2010.11.024>.
- [9] Y. Murakami, T. Kanazaki, Y. Fukushima, H. Tanaka, J. Tomuro, K. Kuboyama, et al., Failure analysis of SUS316L flexible hose for hydrogen station and fatigue life prediction method, *Transactions of the Japan Society of Mechanical Engineers Series A* 75 (2009) 93-102. <http://doi.org/10.1299/kikaia.75.93>.
- [10] T. Michler, C. San Marchi, J. Naumann, S. Weber, M. Martin, Hydrogen environment embrittlement of stable austenitic steels, *Int. J. Hydrogen Energy* 37(21) (2012) 16231-16246. <https://doi.org/10.1016/j.ijhydene.2012.08.071>.
- [11] K.E. Nygren, The influence of hydrogen on the evolving microstructure during fatigue crack growth in metastable and stable austenitic stainless steels, Ph.D. dissertation, Department of Materials Science and Engineering, University of Illinois at Urbana-Champaign (2016).
- [12] C. San Marchi, B.P. Somerday, X. Tang, G.H. Schiroky, Effects of alloy composition and strain hardening on tensile fracture of hydrogen-precharged type 316 stainless steels, *Int. J. Hydrogen Energy* 33(2) (2008) 889-904. <https://doi.org/10.1016/j.ijhydene.2007.10.046>.
- [13] S. Matsuoka, J. Yamabe, H. Matsunaga, Criteria for determining hydrogen compatibility and the mechanisms for hydrogen-assisted, surface crack growth in austenitic stainless steels, *Engin. Frac. Mech.* 153 (2016) 103-127. <https://doi.org/10.1016/j.engfracmech.2015.12.023>.

- [14] C. San Marchi, Hydrogen embrittlement of stainless steels and their welds, *Gaseous Hydrogen Embrittlement of Materials in Energy Technologies*, Woodhead Publishing, 2012, pp. 592-623. <http://doi.org/10.1533/9780857093899.3.592>.
- [15] C.J. McMahon Jr, The role of grain boundaries in hydrogen induced cracking (HIC) of steels, in: R.P. Gangloff, B.P. Somerday (Eds.), *Gaseous Hydrogen Embrittlement of Materials in Energy Technologies*, Woodhead Publishing, 2012, pp. 154-165. <http://doi.org/10.1533/9780857095374.1.154>.
- [16] C. San Marchi, E.S. Hecht, I.W. Ekoto, K.M. Groth, C. LaFleur, B.P. Somerday, et al., Overview of the DOE hydrogen safety, codes and standards program, part 3: Advances in research and development to enhance the scientific basis for hydrogen regulations, codes and standards, *Int. J. Hydrogen Energy* 42(11) (2017) 7263-7274. <https://doi.org/10.1016/j.ijhydene.2016.07.014>.
- [17] J.O.M. Bockris, The Hydrogen Economy, in: J.O.M. Bockris (Ed.), *Environmental Chemistry*, Springer US, Boston, MA, 1977, pp. 549-582. 10.1007/978-1-4615-6921-3_17.
- [18] R. Moliner, M.J. Lázaro, I. Suelves, Analysis of the strategies for bridging the gap towards the Hydrogen Economy, *Int. J. Hydrogen Energy* 41(43) (2016) 19500-19508. <https://doi.org/10.1016/j.ijhydene.2016.06.202>.
- [19] T. Michler, Y. Lee, R.P. Gangloff, J. Naumann, Influence of macro segregation on hydrogen environment embrittlement of SUS 316L stainless steel, *Int. J. Hydrogen Energy* 34(7) (2009) 3201-3209. <https://doi.org/10.1016/j.ijhydene.2009.02.015>.
- [20] T. Michler, J. Naumann, M. Hock, K. Berreth, M.P. Balogh, E. Sattler, Microstructural properties controlling hydrogen environment embrittlement of cold worked 316 type austenitic stainless steels, *Mater. Sci. Eng. A* 628 (2015) 252-261. <https://doi.org/10.1016/j.msea.2015.01.054>.
- [21] L. Zhang, Z. Li, J. Zheng, Y. Zhao, P. Xu, X. Liu, et al., Influence of low temperature prestrain on hydrogen gas embrittlement of metastable austenitic stainless steels, *Int. J. Hydrogen Energy* 38(25) (2013) 11181-11187. <https://doi.org/10.1016/j.ijhydene.2013.01.011>.
- [22] T. DebRoy, H.L. Wei, J.S. Zuback, T. Mukherjee, J.W. Elmer, J.O. Milewski, et al., Additive manufacturing of metallic components – Process, structure and properties, *Prog. Mater. Sci.* 92 (2018) 112-224. <https://doi.org/10.1016/j.pmatsci.2017.10.001>.
- [23] A.J. Birnbaum, J.C. Steuben, E.J. Barrick, A.P. Iliopoulos, J.G. Michopoulos, Intrinsic strain aging, Σ 3 boundaries, and origins of cellular substructure in additively manufactured 316L, *Addit. Manuf.* 29 (2019) 100784. <https://doi.org/10.1016/j.addma.2019.100784>.
- [24] Y.M. Wang, T. Voisin, J.T. McKeown, J. Ye, N.P. Calta, Z. Li, et al., Additively manufactured hierarchical stainless steels with high strength and ductility, *Nat. Mater.* 17 (2017) 63. <https://doi.org/10.1038/nmat5021>.
- [25] T.R. Smith, J.D. Sugar, C. San Marchi, J.M. Schoenung, Strengthening mechanisms in directed energy deposited austenitic stainless steel, *Acta Mater.* 164 (2019) 728-740. <https://doi.org/10.1016/j.actamat.2018.11.021>.
- [26] L. Liu, Q. Ding, Y. Zhong, J. Zou, J. Wu, Y.-L. Chiu, et al., Dislocation network in additive manufactured steel breaks strength–ductility trade-off, *Mater. Today* 21(4) (2018) 354-361. <https://doi.org/10.1016/j.mattod.2017.11.004>.
- [27] C.A. Bronkhorst, J.R. Mayeur, V. Livescu, R. Pokharel, D.W. Brown, G.T. Gray, Structural representation of additively manufactured 316L austenitic stainless steel, *Int. J. Plast.* 118 (2019) 70-86. <https://doi.org/10.1016/j.ijplas.2019.01.012>.

- [28] D.W. Brown, J.D. Bernardin, J.S. Carpenter, B. Clausen, D. Spornjak, J.M. Thompson, Neutron diffraction measurements of residual stress in additively manufactured stainless steel, *Mater. Sci. Eng. A* 678 (2016) 291-298. <https://doi.org/10.1016/j.msea.2016.09.086>.
- [29] R. Pokharel, L. Balogh, D.W. Brown, B. Clausen, G.T. Gray, V. Livescu, et al., Signatures of the unique microstructure of additively manufactured steel observed via diffraction, *Scripta Mater.* 155 (2018) 16-20. <https://doi.org/10.1016/j.scriptamat.2018.06.008>.
- [30] J.A. Brooks, A.J. West, A.W. Thompson, Effect of weld composition and microstructure on hydrogen assisted fracture of austenitic stainless steels, *Metall. Trans. A* 14(1) (1983) 75-84. <https://doi.org/10.1007/BF02643740>.
- [31] H.K. Birnbaum, P. Sofronis, Hydrogen-enhanced localized plasticity—a mechanism for hydrogen-related fracture, *Mater. Sci. Eng. A* 176 (1994) 191. [https://doi.org/10.1016/0921-5093\(94\)90975-X](https://doi.org/10.1016/0921-5093(94)90975-X).
- [32] G. Sander, J. Tan, P. Balan, O. Gharbi, D.R. Feenstra, L. Singer, et al., Corrosion of Additively Manufactured Alloys: A Review, *Corrosion* 74(12) (2018) 1318-1350. www.doi.org/10.5006/2926.
- [33] S.-W. Baek, E.J. Song, J.H. Kim, M. Jung, U.B. Baek, S.H. Nahm, Hydrogen embrittlement of 3-D printing manufactured austenitic stainless steel part for hydrogen service, *Scripta Mater.* 130 (2017) 87-90. <https://doi.org/10.1016/j.scriptamat.2016.11.020>.
- [34] Y. Hong, C. Zhou, Y. Zheng, L. Zhang, J. Zheng, X. Chen, et al., Formation of strain-induced martensite in selective laser melting austenitic stainless steel, *Mater. Sci. Eng. A* 740-741 (2019) 420-426. <https://doi.org/10.1016/j.msea.2018.10.121>.
- [35] D. Kong, C. Dong, X. Ni, L. Zhang, H. Luo, R. Li, et al., Superior resistance to hydrogen damage for selective laser melted 316L stainless steel in a proton exchange membrane fuel cell environment, *Corros. Sci.* 166 (2020) 108425. <https://doi.org/10.1016/j.corsci.2019.108425>.
- [36] M. Koyama, S. Okazaki, T. Sawaguchi, K. Tsuzaki, Hydrogen embrittlement susceptibility of Fe-Mn binary alloys with high Mn content: effects of stable and metastable ϵ -martensite, and Mn concentration, *Metall. Mater. Trans. A* 47(6) (2016) 2656-2673. <https://doi.org/10.1007/s11661-016-3431-9>.
- [37] L. Zhang, Z. Li, J. Zheng, Y. Zhao, P. Xu, C. Zhou, et al., Effect of strain-induced martensite on hydrogen embrittlement of austenitic stainless steels investigated by combined tension and hydrogen release methods, *Int. J. Hydrogen Energy* 38(19) (2013) 8208-8214. <https://doi.org/10.1016/j.ijhydene.2013.01.198>.
- [38] B. Rankouhi, K.M. Bertsch, G. Meric de Bellefon, M. Thevamaran, D.J. Thoma, K. Suresh, Experimental validation and microstructure characterization of topology optimized, additively manufactured SS316L components, *Mater. Sci. Eng. A* 776 (2020) 139050. <https://doi.org/10.1016/j.msea.2020.139050>.
- [39] K.M. Bertsch, G. Meric de Bellefon, B. Kuehl, D.J. Thoma, Origin of dislocation structures in an additively manufactured austenitic stainless steel 316L, *Acta Mater.* 199 (2020) 19-33. <https://doi.org/10.1016/j.actamat.2020.07.063>.
- [40] H. Fayazfar, M. Salarian, A. Rogalsky, D. Sarker, P. Russo, V. Paserin, et al., A critical review of powder-based additive manufacturing of ferrous alloys: Process parameters, microstructure and mechanical properties, *Mater. Des.* 144 (2018) 98-128. <https://doi.org/10.1016/j.matdes.2018.02.018>.
- [41] E.J. Schindelholz, M.A. Melia, J.M. Rodelas, Corrosion of Additively Manufactured Stainless Steels—Process, Structure, Performance: A Review, *Corrosion* 77(5) (2021) 484-503. www.doi.org/10.5006/3741.

- [42] D. Peckner, I.M. Bernstein, Handbook of stainless steels, McGraw-Hill, New York, 1977.
- [43] T. Angel, Formation of martensite in austenitic stainless steels, Journal of the Iron and Steel Institute 177 (1954) 165-174.
- [44] G. Meric de Bellefon, K.M. Bertsch, M.R. Chancey, Y.Q. Wang, D.J. Thoma, Influence of solidification structures on radiation-induced swelling in an additively-manufactured austenitic stainless steel, J. Nucl. Mater. 523 (2019) 291-298.
<https://doi.org/10.1016/j.jnucmat.2019.06.012>.
- [45] B. Rankouhi, A.K. Agrawal, F.E. Pfefferkorn, D.J. Thoma, A dimensionless number for predicting universal processing parameter boundaries in metal powder bed additive manufacturing, Manufacturing Letters 27 (2021) 13-17.
<https://doi.org/10.1016/j.mfglet.2020.12.002>.
- [46] F. Bachmann, R. Hielscher, H. Schaeben, Grain detection from 2d and 3d EBSD data—Specification of the MTEX algorithm, Ultramicroscopy 111(12) (2011) 1720-1733.
<https://doi.org/10.1016/j.ultramic.2011.08.002>.
- [47] M.R. Louthan, R.G. Derrick, Hydrogen transport in austenitic stainless steel, Corros. Sci. 15(6) (1975) 565-577. [https://doi.org/10.1016/0010-938X\(75\)90022-0](https://doi.org/10.1016/0010-938X(75)90022-0).
- [48] C. San Marchi, T. Michler, K.A. Nibur, B.P. Somerday, On the physical differences between tensile testing of type 304 and 316 austenitic stainless steels with internal hydrogen and in external hydrogen, Int. J. Hydrogen Energy 35(18) (2010) 9736-9745.
<https://doi.org/10.1016/j.ijhydene.2010.06.018>.
- [49] A. Nagao, M. Dadfarnia, B.P. Somerday, P. Sofronis, R.O. Ritchie, Hydrogen-enhanced-plasticity mediated decohesion for hydrogen-induced intergranular and “quasi-cleavage” fracture of lath martensitic steels, J. Mech. Phys. Solids 112 (2018) 403-430.
<https://doi.org/10.1016/j.jmps.2017.12.016>.
- [50] M. Koyama, E. Akiyama, T. Sawaguchi, K. Ogawa, I.V. Kireeva, Y.I. Chumlyakov, et al., Hydrogen-assisted quasi-cleavage fracture in a single crystalline type 316 austenitic stainless steel, Corros. Sci. 75 (2013) 345-353. <https://doi.org/10.1016/j.corsci.2013.06.018>.
- [51] J.M. Rigsbee, R.B. Benson, A TEM investigation of hydrogen-induced deformation twinning and associated martensitic phases in 304-type stainless steel, Journal of Materials Science 12(2) (1977) 406-409. <https://doi.org/10.1007/bf00566284>.
- [52] D.L. Holt, Dislocation cell formation in metals, J. Appl. Phys. 41(8) (1970) 3197-3201.
<https://doi.org/10.1063/1.1659399>.
- [53] M.R. Staker, D.L. Holt, The dislocation cell size and dislocation density in copper deformed at temperatures between 25 and 700°C, Acta Metall. 20(4) (1972) 569-579.
[https://doi.org/10.1016/0001-6160\(72\)90012-0](https://doi.org/10.1016/0001-6160(72)90012-0).
- [54] K.M. Bertsch, S. Wang, A. Nagao, I.M. Robertson, Hydrogen-induced compatibility constraints across grain boundaries drive intergranular failure of Ni, Mater. Sci. Eng. A 760 (2019) 58-67. <https://doi.org/10.1016/j.msea.2019.05.036>.
- [55] S. Wang, A. Nagao, K. Edalati, Z. Horita, I.M. Robertson, Influence of hydrogen on dislocation self-organization in Ni, Acta Mater. 135(Supplement C) (2017) 96-102.
<https://doi.org/10.1016/j.actamat.2017.05.073>.
- [56] D.W. Gross, The microstructural evolution of fatigue cracks in fcc metals, Ph.D. thesis, Mater. Sci. Eng., University of Illinois at Urbana-Champaign (2016).
- [57] J.R. Buckley, D. Hardie, The effect of pre-straining and δ -ferrite on the embrittlement of 304L stainless steel by hydrogen, Corros. Sci. 34(1) (1993) 93-107.
[https://doi.org/10.1016/0010-938X\(93\)90261-E](https://doi.org/10.1016/0010-938X(93)90261-E).

- [58] C. Zhou, Y. Song, Q. Shi, S. Hu, J. Zheng, P. Xu, et al., Effect of pre-strain on hydrogen embrittlement of metastable austenitic stainless steel under different hydrogen conditions, *Int. J. Hydrogen Energy* 44(47) (2019) 26036-26048. <https://doi.org/10.1016/j.ijhydene.2019.08.046>.
- [59] I.-J. Park, J.-G. Jung, S.Y. Jo, S.-M. Lee, Y.-K. Lee, The effect of pre-strain on the resistance to hydrogen embrittlement in 316L austenitic stainless steel, *Materials Transactions* 55(6) (2014) 964-970. www.doi.org/10.2320/matertrans.M2014036.
- [60] Y. Wang, X. Wang, J. Gong, L. Shen, W. Dong, Hydrogen embrittlement of cathodically hydrogen-precharged 304L austenitic stainless steel: Effect of plastic pre-strain, *Int. J. Hydrogen Energy* 39(25) (2014) 13909-13918. <https://doi.org/10.1016/j.ijhydene.2014.04.122>.
- [61] T. Matsuo, J. Yamabe, S. Matsuoka, Effects of hydrogen on tensile properties and fracture surface morphologies of Type 316L stainless steel, *Int. J. Hydrogen Energy* 39(7) (2014) 3542-3551. <https://doi.org/10.1016/j.ijhydene.2013.12.099>.
- [62] M.R. Louthan, G.R. Caskey, J.A. Donovan, D.E. Rawl, Hydrogen embrittlement of metals, *Mater. Sci. Eng.* 10 (1972) 357-368. [https://doi.org/10.1016/0025-5416\(72\)90109-7](https://doi.org/10.1016/0025-5416(72)90109-7).
- [63] L. Chen, X. Xiong, X. Tao, Y. Su, L. Qiao, Effect of dislocation cell walls on hydrogen adsorption, hydrogen trapping and hydrogen embrittlement resistance, *Corros. Sci.* 166 (2020) 108428. <https://doi.org/10.1016/j.corsci.2020.108428>.
- [64] I.M. Robertson, The effect of hydrogen on dislocation dynamics, *Engin. Frac. Mech.* 68(6) (2001) 671-692. [http://doi.org/10.1016/S0013-7944\(01\)00011-X](http://doi.org/10.1016/S0013-7944(01)00011-X).
- [65] I.M. Robertson, M.L. Martin, J.A. Fenske, Influence of hydrogen on the behavior of dislocations, in: R.P. Gangloff, B.P. Somerday (Eds.), *Gaseous Hydrogen Embrittlement of Materials in Energy Technologies*, Woodhead Publishing, 2012, pp. 166-206. <http://doi.org/10.1533/9780857095374.1.166>.
- [66] P.J. Ferreira, I.M. Robertson, H.K. Birnbaum, Hydrogen effects on the character of dislocations in high-purity aluminum, *Acta Mater.* 47 (1999) 2991. [https://doi.org/10.1016/S1359-6454\(99\)00156-1](https://doi.org/10.1016/S1359-6454(99)00156-1).
- [67] K.A. Nibur, D.F. Bahr, B.P. Somerday, Hydrogen effects on dislocation activity in austenitic stainless steel, *Acta Mater.* 54(10) (2006) 2677-2684. <https://doi.org/10.1016/j.actamat.2006.02.007>.
- [68] D.P. Abraham, C.J. Altstetter, Hydrogen-enhanced localization of plasticity in an austenitic stainless steel, *Metall. Mater. Trans. A* 26(11) (1995) 2859-2871. <https://doi.org/10.1007/bf02669644>.
- [69] D.G. Ulmer, C.J. Altstetter, Hydrogen-induced strain localization and failure of austenitic stainless steels at high hydrogen concentrations, *Acta Metallurgica et Materialia* 39(6) (1991) 1237-1248. [http://dx.doi.org/10.1016/0956-7151\(91\)90211-I](http://dx.doi.org/10.1016/0956-7151(91)90211-I).
- [70] K.A. Nibur, B.P. Somerday, D.K. Balch, C. San Marchi, The role of localized deformation in hydrogen-assisted crack propagation in 21Cr-6Ni-9Mn stainless steel, *Acta Mater.* 57(13) (2009) 3795-3809. <https://doi.org/10.1016/j.actamat.2009.04.027>.
- [71] G. Girardin, C. Huvier, D. Delafosse, X. Feaugas, Correlation between dislocation organization and slip bands: TEM and AFM investigations in hydrogen-containing nickel and nickel-chromium, *Acta Mater.* 91 (2015) 141-151. <http://dx.doi.org/10.1016/j.actamat.2015.03.016>.
- [72] P.J. Ferreira, Hydrogen effects on crystal dislocations and stacking-fault energy, Ph.D. dissertation, Department of Materials Science and Engineering, University of Illinois at Urbana-Champaign (1988).

- [73] J.E.C. Sabisch, J.D. Sugar, J. Ronevich, C. San Marchi, D.L. Medlin, Interrogating the effects of hydrogen on the behavior of planar deformation bands in austenitic stainless steel, *Metall. Mater. Trans. A* (2021). www.doi.org/10.1007/s11661-021-06170-3.
- [74] P. Rozenak, I.M. Robertson, H.K. Birnbaum, HVEM studies of the effects of hydrogen on the deformation and fracture of AISI type 316 austenitic stainless steel, *Acta Metallurgica et Materialia* 38(11) (1990) 2031-2040. [https://doi.org/10.1016/0956-7151\(90\)90070-W](https://doi.org/10.1016/0956-7151(90)90070-W).
- [75] A.M. Brass, J. Chêne, Hydrogen uptake in 316L stainless steel: Consequences on the tensile properties, *Corros. Sci.* 48(10) (2006) 3222-3242. <https://doi.org/10.1016/j.corsci.2005.11.004>.
- [76] J. Albrecht, I.M. Bernstein, A.W. Thompson, Evidence for dislocation transport of hydrogen in aluminum, *Metall. Trans. A* 13(5) (1982) 811-820. <https://doi.org/10.1007/bf02642394>.
- [77] M. Kurkela, R.M. Latanision, The effect of plastic deformation on the transport of hydrogen in nickel, *Scr. Metall.* 13(10) (1979) 927-932. [http://dx.doi.org/10.1016/0036-9748\(79\)90322-3](http://dx.doi.org/10.1016/0036-9748(79)90322-3).
- [78] S. Wang, M.L. Martin, P. Sofronis, S. Ohnuki, N. Hashimoto, I.M. Robertson, Hydrogen-induced intergranular failure of iron, *Acta Mater.* 69 (2014) 275-282. <http://doi.org/10.1016/j.actamat.2014.01.060>.
- [79] K.E. Nygren, S. Wang, K.M. Bertsch, H. Bei, A. Nagao, I.M. Robertson, Hydrogen embrittlement of the equi-molar FeNiCoCr alloy *Acta Mater.* 157 (2018) 218-227. <https://doi.org/10.1016/j.actamat.2018.07.032>.
- [80] S. Kibey, J.B. Liu, D.D. Johnson, H. Sehitoglu, Predicting twinning stress in fcc metals: Linking twin-energy pathways to twin nucleation, *Acta Mater.* 55(20) (2007) 6843-6851. <https://doi.org/10.1016/j.actamat.2007.08.042>.
- [81] S. Mahajan, Deformation Twinning, *Encyclopedia of Materials: Science and Technology* (Second Edition), Elsevier, Oxford, 2002, pp. 1-14. <https://doi.org/10.1016/B0-08-043152-6/01809-X>.
- [82] M.A. Meyers, O. Vöhringer, V.A. Lubarda, The onset of twinning in metals: a constitutive description, *Acta Mater.* 49(19) (2001) 4025-4039. [https://doi.org/10.1016/S1359-6454\(01\)00300-7](https://doi.org/10.1016/S1359-6454(01)00300-7).
- [83] M. Koyama, E. Akiyama, K. Tsuzaki, D. Raabe, Hydrogen-assisted failure in a twinning-induced plasticity steel studied under in situ hydrogen charging by electron channeling contrast imaging, *Acta Mater.* 61(12) (2013) 4607-4618. <https://doi.org/10.1016/j.actamat.2013.04.030>.
- [84] K.M. Bertsch, K.E. Nygren, S. Wang, H. Bei, A. Nagao, Hydrogen-enhanced compatibility constraint for intergranular failure in FCC FeNiCoCrMn high-entropy alloy, *Corros. Sci.* 184 (2021) 109407. <https://doi.org/10.1016/j.corsci.2021.109407>.
- [85] S. Wang, K.E. Nygren, A. Nagao, P. Sofronis, I.M. Robertson, On the failure of surface damage to assess the hydrogen-enhanced deformation ahead of crack tip in a cyclically loaded austenitic stainless steel, *Scripta Mater.* 166 (2019) 102-106. <https://doi.org/10.1016/j.scriptamat.2019.03.010>.
- [86] B.C. Odegard, A.J. West, On the thermo-mechanical behavior and hydrogen compatibility of 22-13-5 stainless steel, *Mater. Sci. Eng.* 19(2) (1975) 261-269. [https://doi.org/10.1016/0025-5416\(75\)90113-5](https://doi.org/10.1016/0025-5416(75)90113-5).
- [87] K. Saeidi, F. Akhtar, Subgrain-controlled grain growth in the laser-melted 316 L promoting strength at high temperatures, *Royal Society Open Science* 5(5) (2018) 172394. www.doi.org/10.1098/rsos.172394.
- [88] T.R. Smith, J.D. Sugar, J.M. Schoenung, C. San Marchi, Anomalous annealing response of directed energy deposited type 304L austenitic stainless steel, *JOM* 70(3) (2018) 358-363. www.doi.org/10.1007/s11837-017-2711-1.

- [89] T. Voisin, J.-B. Forien, A. Perron, S. Aubry, N. Bertin, A. Samanta, et al., New insights on cellular structures strengthening mechanisms and thermal stability of an austenitic stainless steel fabricated by laser powder-bed-fusion, *Acta Mater.* 203 (2021) 116476. <https://doi.org/10.1016/j.actamat.2020.11.018>.
- [90] A.J. West, M.R. Louthan, Dislocation transport and hydrogen embrittlement, *Metall. Trans. A* 10(11) (1979) 1675-1682. <https://doi.org/10.1007/BF02811700>.
- [91] K.E. Nygren, K.M. Bertsch, S. Wang, H. Bei, A. Nagao, I.M. Robertson, Hydrogen embrittlement in compositionally complex FeNiCoCrMn FCC solid solution alloy, *Curr. Opin. Solid State Mater. Sci.* 22(1) (2018) 1-7. <https://doi.org/10.1016/j.cossms.2017.11.002>.
- [92] G. Winther, Slip systems extracted from lattice rotations and dislocation structures, *Acta Mater.* 56(9) (2008) 1919-1932. <http://dx.doi.org/10.1016/j.actamat.2007.12.026>.
- [93] D. Barbier, N. Gey, S. Allain, N. Bozzolo, M. Humbert, Analysis of the tensile behavior of a TWIP steel based on the texture and microstructure evolutions, *Mater. Sci. Eng. A* 500(1) (2009) 196-206. <https://doi.org/10.1016/j.msea.2008.09.031>.
- [94] S. Sevsek, F. Brasche, D.A. Molodov, W. Bleck, On the influence of grain size on the TWIP/TRIP-effect and texture development in high-manganese steels, *Mater. Sci. Eng. A* 754 (2019) 152-160. <https://doi.org/10.1016/j.msea.2019.03.072>.
- [95] R.E. Schramm, R.P. Reed, Stacking fault energies of seven commercial austenitic stainless steels, *Metall. Trans. A* 6(7) (1975) 1345. <https://doi.org/10.1007/bf02641927>.
- [96] L. Vitos, J.O. Nilsson, B. Johansson, Alloying effects on the stacking fault energy in austenitic stainless steels from first-principles theory, *Acta Mater.* 54(14) (2006) 3821-3826. <https://doi.org/10.1016/j.actamat.2006.04.013>.
- [97] H.K. Birnbaum, P. Sofronis, Hydrogen-enhanced localized plasticity—a mechanism for hydrogen-related fracture, *Mater. Sci. Eng. A* A176(1- 2) (1994) 191-202. [http://dx.doi.org/10.1016/0921-5093\(94\)90975-X](http://dx.doi.org/10.1016/0921-5093(94)90975-X).
- [98] A. Kimura, H.K. Birnbaum, Hydrogen induced grain boundary fracture in high purity nickel and its alloys—Enhanced hydrogen diffusion along grain boundaries, *Acta Metall.* 36(3) (1988) 757-766. [http://dx.doi.org/10.1016/0001-6160\(88\)90109-5](http://dx.doi.org/10.1016/0001-6160(88)90109-5).
- [99] L.W. Tsay, H.L. Lu, C. Chen, The effect of grain size and aging on hydrogen embrittlement of a maraging steel, *Corros. Sci.* 50(9) (2008) 2506-2511. <https://doi.org/10.1016/j.corsci.2008.06.044>.
- [100] Y.-C. Lin, D. Chen, M.-H. Chiang, G.-J. Cheng, H.-C. Lin, H.-W. Yen, Response of hydrogen desorption and hydrogen embrittlement to precipitation of nanometer-sized copper in tempered martensitic low-carbon steel, *Journal of Materials* 71(4) (2019) 1349-1356. www.doi.org/10.1007/s11837-019-03330-0.
- [101] T. Hickel, R. Nazarov, E.J. McEniry, G. Leyson, B. Grabowski, J. Neugebauer, Ab initio based understanding of the segregation and diffusion mechanisms of hydrogen in steels, *Journal of Materials* 66(8) (2014) 1399-1405. <https://doi.org/10.1007/s11837-014-1055-3>.
- [102] A. Nagao, M.L. Martin, M. Dadfarnia, P. Sofronis, I.M. Robertson, The effect of nano-sized (Ti, Mo)C precipitates on hydrogen embrittlement of tempered lath martensitic steel, *Acta Mater.* 74 (2014) 244. <https://doi.org/10.1016/j.actamat.2014.04.051>.
- [103] Z. Tarzimoghadam, D. Ponge, J. Klöwer, D. Raabe, Hydrogen-assisted failure in Ni-based superalloy 718 studied under in situ hydrogen charging: The role of localized deformation in crack propagation, *Acta Mater.* 128 (2017) 365-374. <https://doi.org/10.1016/j.actamat.2017.02.059>.

- [104] R.W. Bauer, H.G.F. Wilsdorf, Void initiation in ductile fracture, *Scr. Metall.* 7(11) (1973) 1213-1220. [https://doi.org/10.1016/0036-9748\(73\)90250-0](https://doi.org/10.1016/0036-9748(73)90250-0).
- [105] G. Le Roy, J.D. Embury, G. Edwards, M.F. Ashby, A model of ductile fracture based on the nucleation and growth of voids, *Acta Metall.* 29(8) (1981) 1509-1522. [https://doi.org/10.1016/0001-6160\(81\)90185-1](https://doi.org/10.1016/0001-6160(81)90185-1).
- [106] P. Noell, J. Carroll, K. Hattar, B. Clark, B. Boyce, Do voids nucleate at grain boundaries during ductile rupture?, *Acta Mater.* 137(Supplement C) (2017) 103-114. <https://doi.org/10.1016/j.actamat.2017.07.004>.
- [107] C. Landron, E. Maire, O. Bouaziz, J. Adrien, L. Lecarme, A. Bareggi, Validation of void growth models using X-ray microtomography characterization of damage in dual phase steels, *Acta Mater.* 59(20) (2011) 7564-7573. <https://doi.org/10.1016/j.actamat.2011.08.046>.
- [108] A.A. Benzerga, J.-B. Leblond, Ductile fracture by void growth to coalescence, in: H. Aref, E.v.d. Giessen (Eds.), *Advances in Applied Mechanics*, Elsevier, 2010, pp. 169-305. [https://doi.org/10.1016/S0065-2156\(10\)44003-X](https://doi.org/10.1016/S0065-2156(10)44003-X).
- [109] M. Nagumo, Conformity between mechanics and microscopic functions of hydrogen in failure, *ISIJ Int.* 52(2) (2012) 168-173. <https://doi.org/10.2355/isijinternational.52.168>.
- [110] M. Nagumo, Hydrogen related failure of steels – a new aspect, *Mater. Sci. Technol.* 20(8) (2004) 940-950. www.dog.org/10.1179/026708304225019687.
- [111] M. Nagumo, M. Nakamura, K. Takai, Hydrogen thermal desorption relevant to delayed-fracture susceptibility of high-strength steels, *Metall. Mater. Trans. A* 32A (2001) 339. <https://doi.org/10.1007/s11661-001-0265-9>.

9. Figure Captions

Figure 1. Thermal desorption analysis of uncharged (open symbols) and hydrogen-charged (filled symbols) parts, both SLM (circles) and DED (squares). As-built (AB) parts shown in black, heat-treated (HT) shown in gray.

Figure 2. Engineering stress-strain curves for selected specimens of a. SLM and b. DED materials. Thin curves represent as-built materials (black for uncharged, red for hydrogen-charged), thicker curves represent heat-treated materials (gray for uncharged, pink for hydrogen-charged), for both a and b. Color online.

Figure 3. SEM fractographs of dimples on the fracture surfaces of a, e. SLM as-built, b, f. SLM heat-treated, c, g. DED as-built, and d, h. DED heat-treated materials. a-d (top row) uncharged, e-h (bottom row) hydrogen-charged.

Figure 4. Bright-field STEM micrographs of microstructures underneath the fracture surfaces in a, e. SLM as-built, b, f. SLM heat-treated, c, g. DED as-built, and d, h. DED heat-treated materials. a-d (top row) uncharged, e-h (bottom row) hydrogen-charged. Arrowheads indicate voids. In e., solid black lines highlight twins and an arrow highlights a step on the fracture surface. Fracture surfaces shown at the top of each image; tensile axis is vertical.

Figure 5. Average void diameter and number density for uncharged (open symbols) and hydrogen-charged (filled symbols) materials. SLM material indicated by circles, DED indicated by squares. As-built materials shown in black, heat-treated materials shown in gray.

Figure 6. Bright-field STEM micrographs of dislocation structures at 15% elongation in a, b. SLM as-built, and c, d. DED as-built materials. Dashed line in b. parallel to deformation twins, dotted lines in c. and d. indicate dislocation cell walls with dendritic segregation profiles.

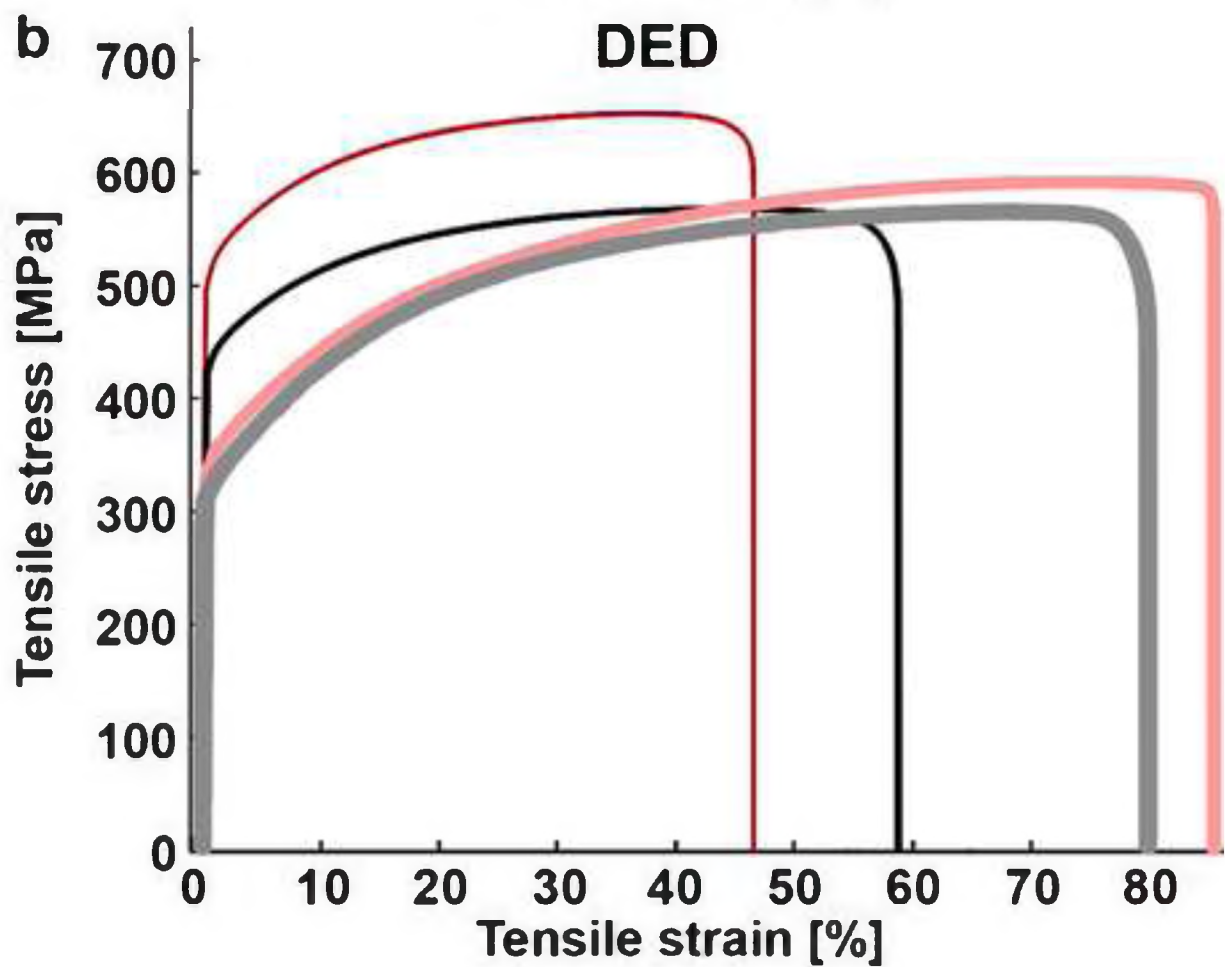
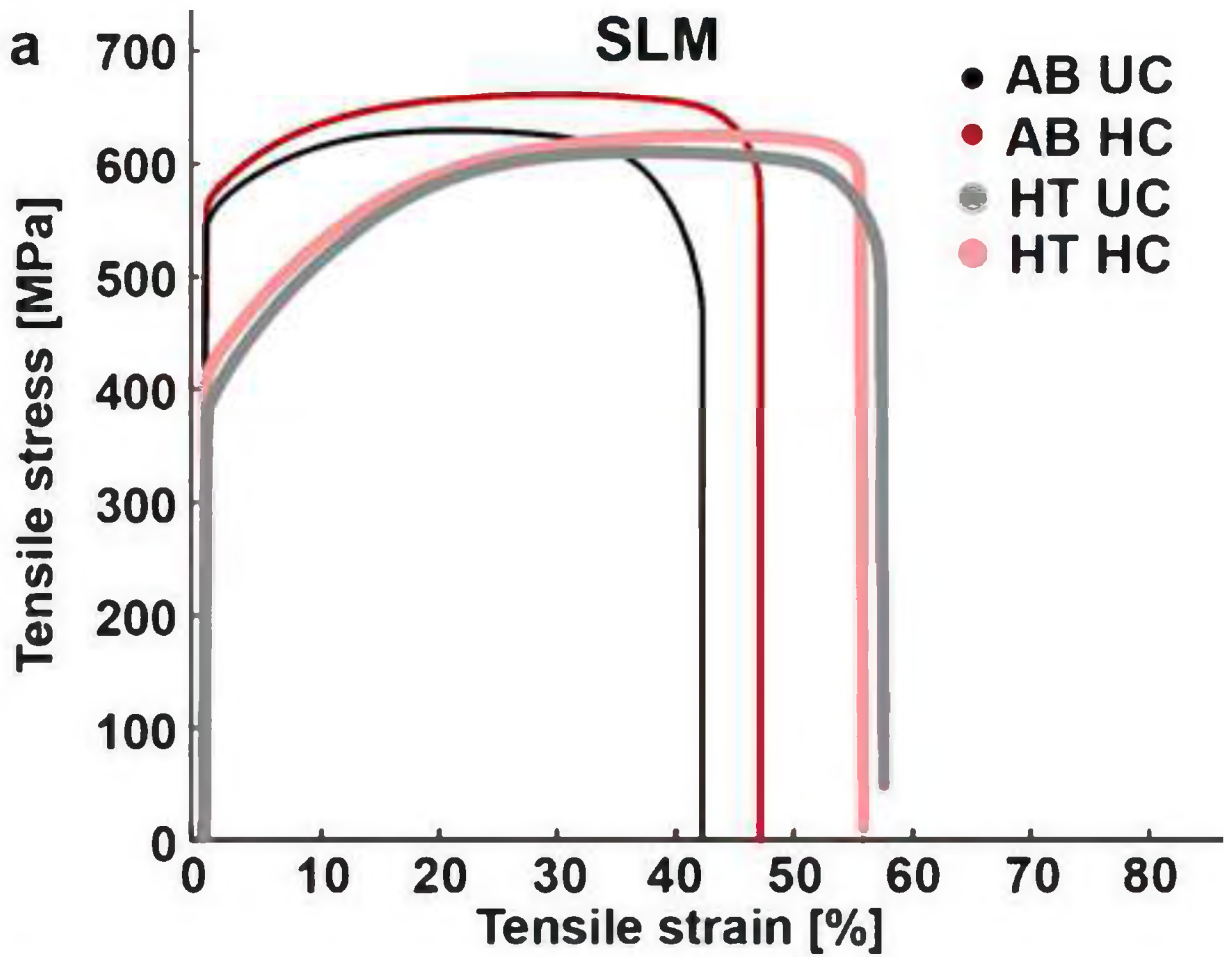
Figure 7. Bright-field STEM micrographs (top row) and misorientation maps (bottom row) in a, c. uncharged SLM as-built and b, d. hydrogen-charged SLM as-built materials. The free surface is at the top, and the tensile axis is approximately horizontal. In a., arrow indicates curved deformation bands, crossed lines are parallel to different twinning systems, and D represents a twin-free region with dislocation cells. In c, d., reference points indicated by black dots with white outlines; grain boundaries shown in thick black, deformation boundaries with local misorientation 3° or greater in thin black, twin boundaries in thick red. Color online.

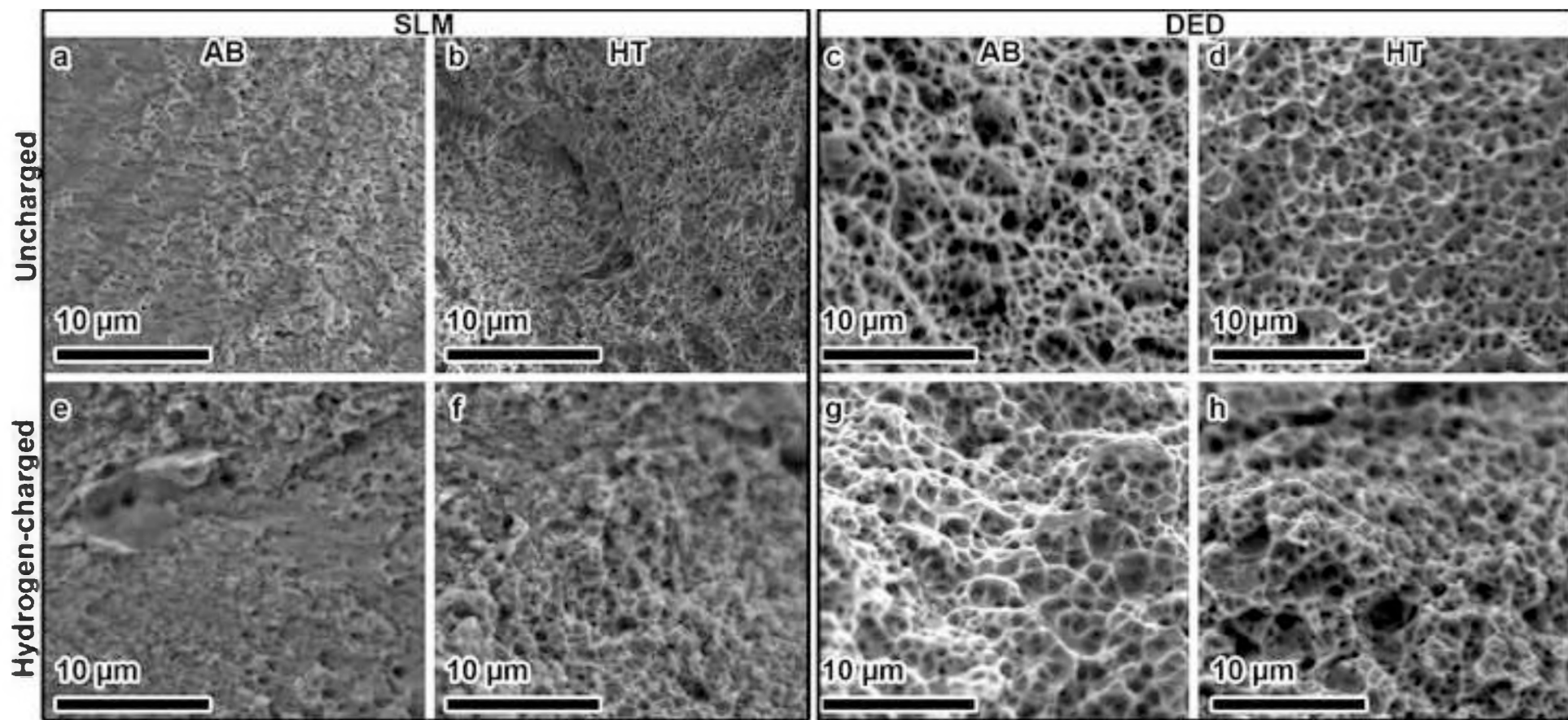
Figure 8. Bright-field STEM micrographs of dislocation structures up to 250 μm away from the fracture surfaces in a. uncharged SLM as-built and b. hydrogen-charged SLM as-built materials. Arrows indicate voids formed along dislocation walls.

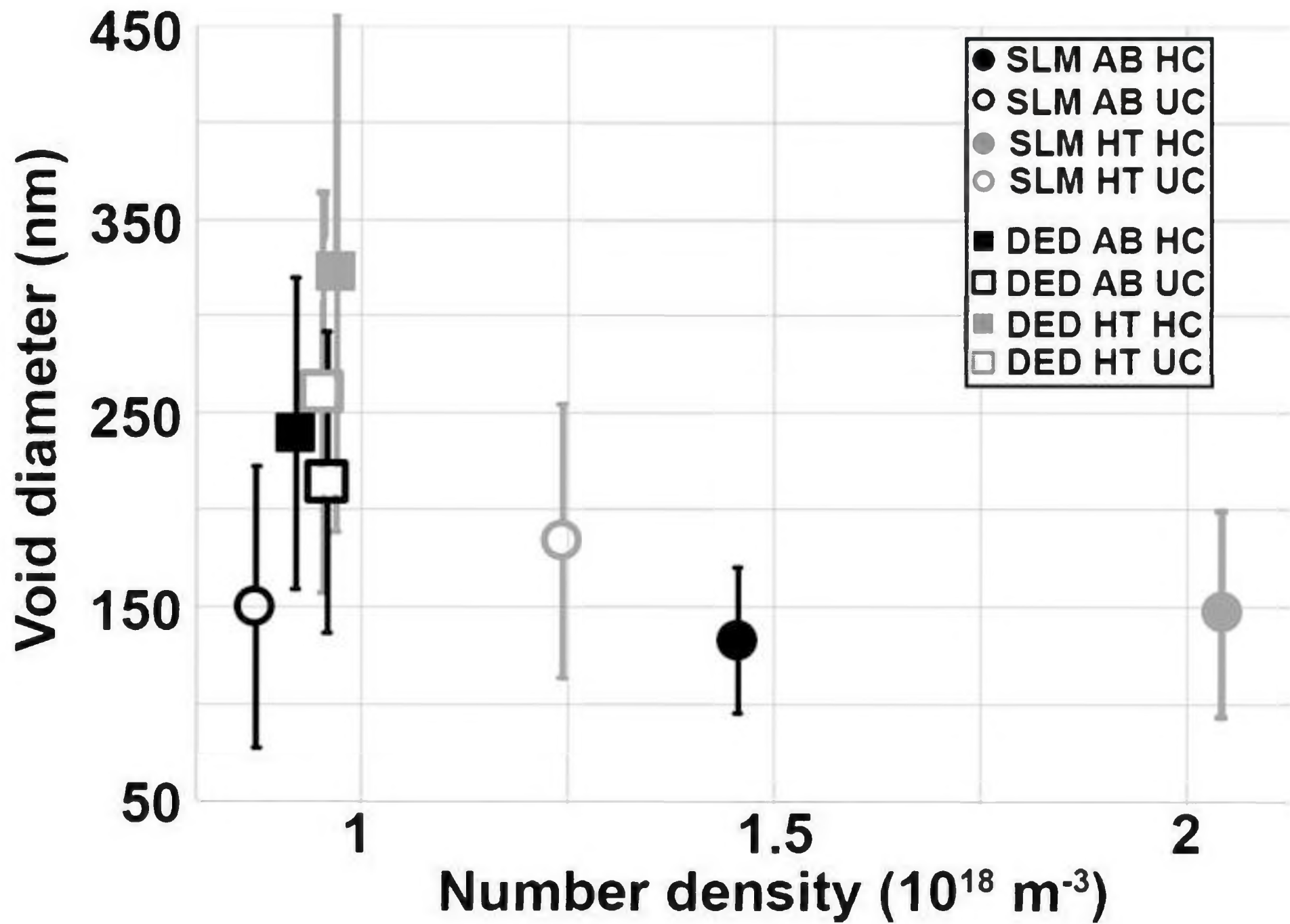
Figure 9. Bright-field STEM micrographs (top row) and t-EBSD misorientation maps (bottom row) in a, c. uncharged DED as-built and b, d. hydrogen-charged DED as-built materials. The free surface is at the top of images, and the tensile axis is approximately horizontal. In a, b., black lines with white outlines are parallel to different twinning systems. In c, d., reference points are indicated by black dots with white outlines; grain boundaries shown in thick black, twin boundaries in thick red. Color online.

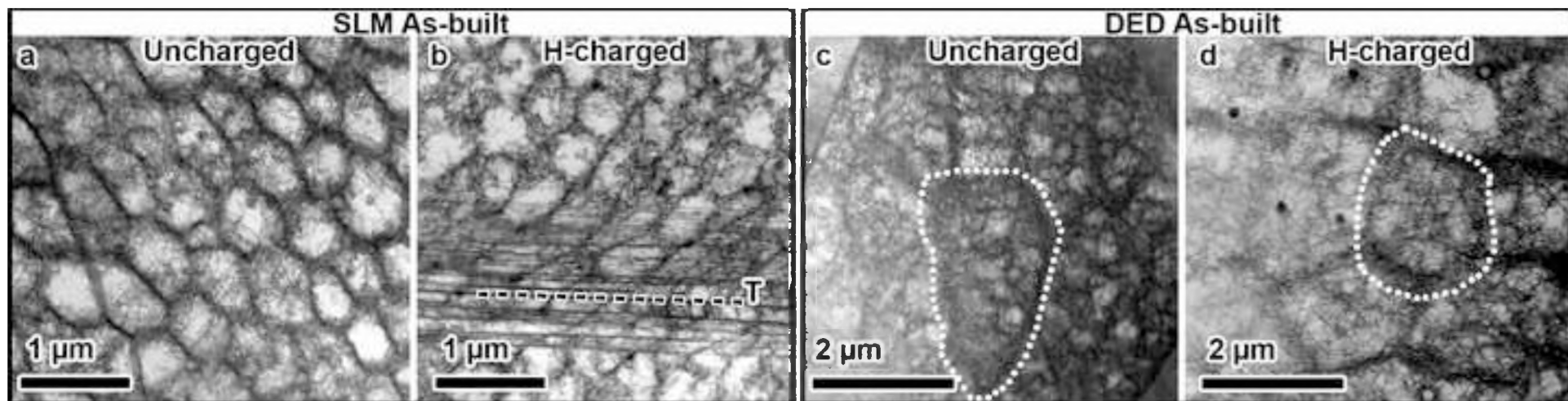
Figure 10. Bright-field STEM micrographs of dislocation structures up to 250 μm away from the fracture surfaces in a. uncharged DED as-built and b. hydrogen-charged DED as-built materials. Arrows indicate voids formed along dislocation walls. Dashed lines show deformation bands. A dotted white circle in b. indicates a well-defined dislocation cell.

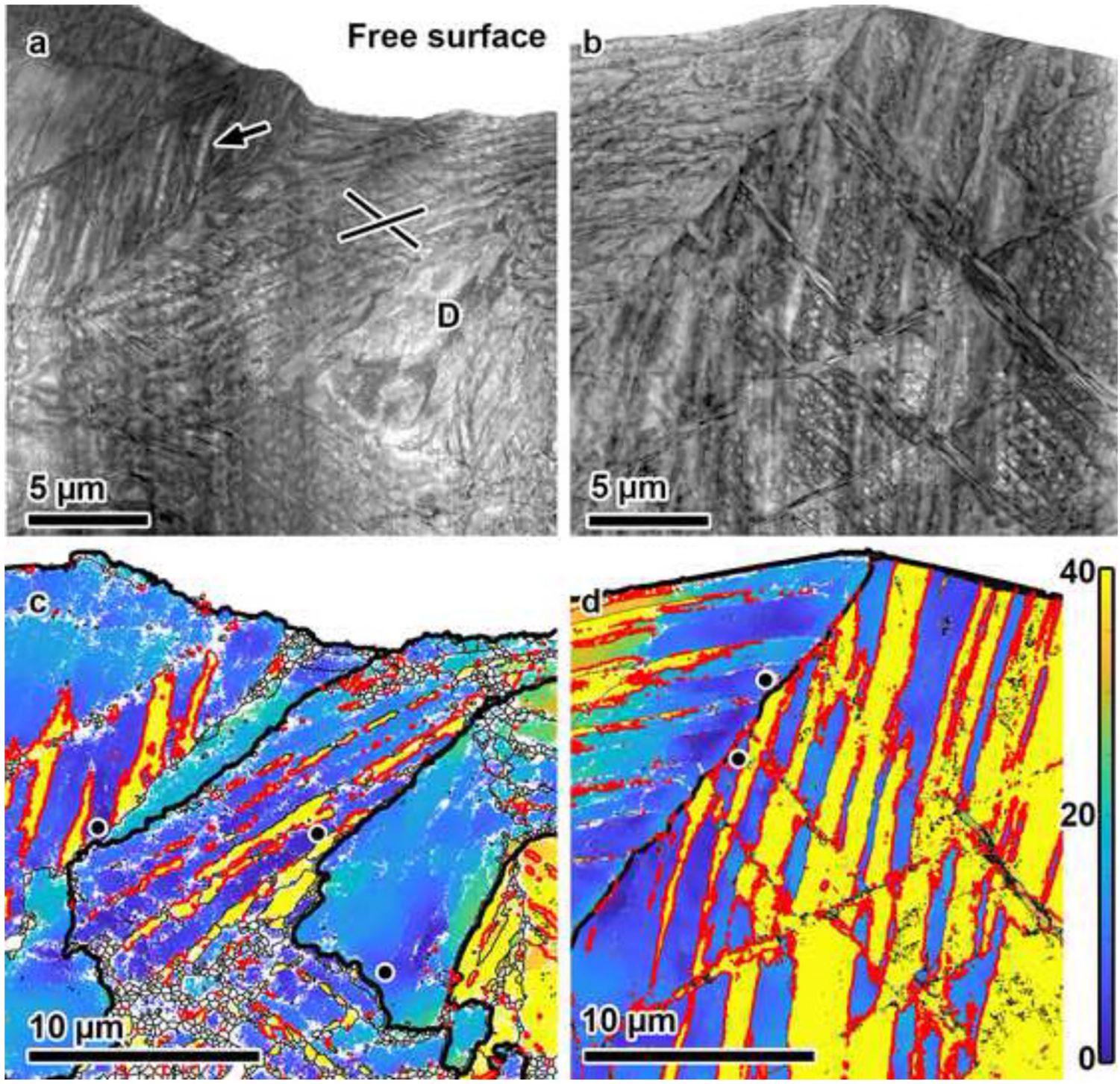
Figure 11. EBSD maps and stereographic triangle inverse pole figures representing texture in a. uncharged SLM as-built, b. hydrogen-charged SLM as-built, c. uncharged DED as-built, and d. hydrogen-charged DED as-built materials. Maps colorized according to the crystallographic orientation in the tensile direction (vertical in maps), and the color keys shown in the stereographic triangles. An arrow in d. indicates deformation twinning. Color online.

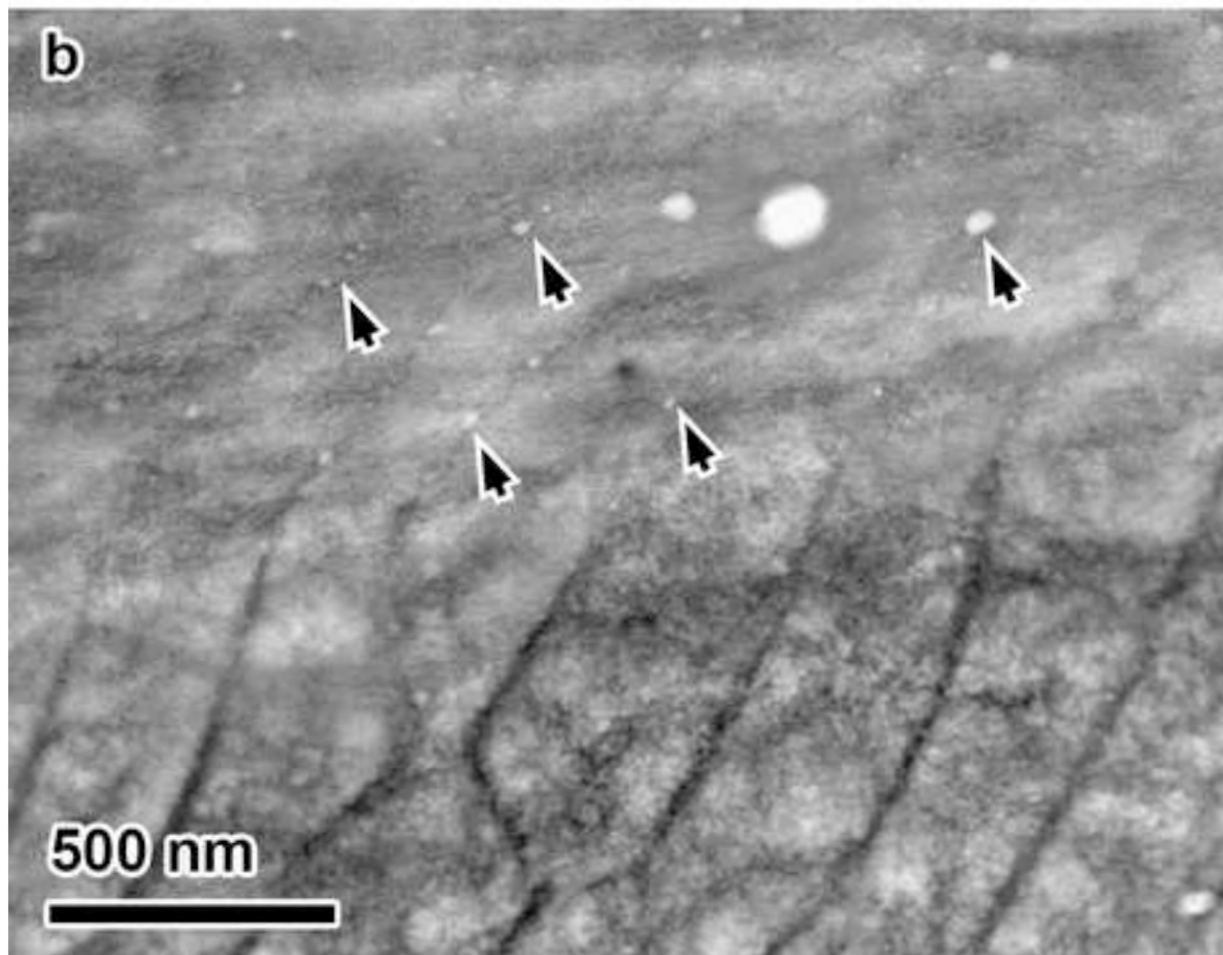
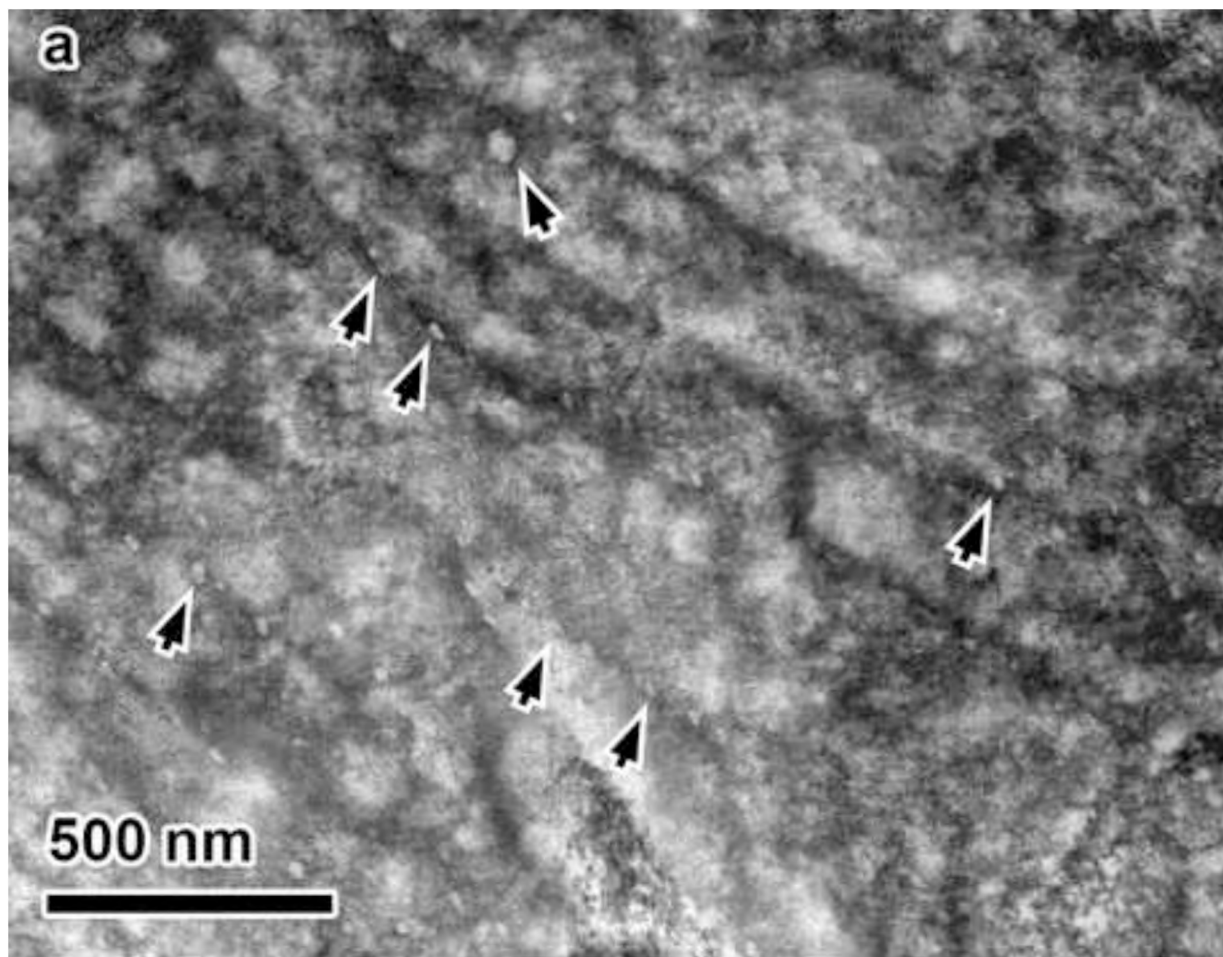


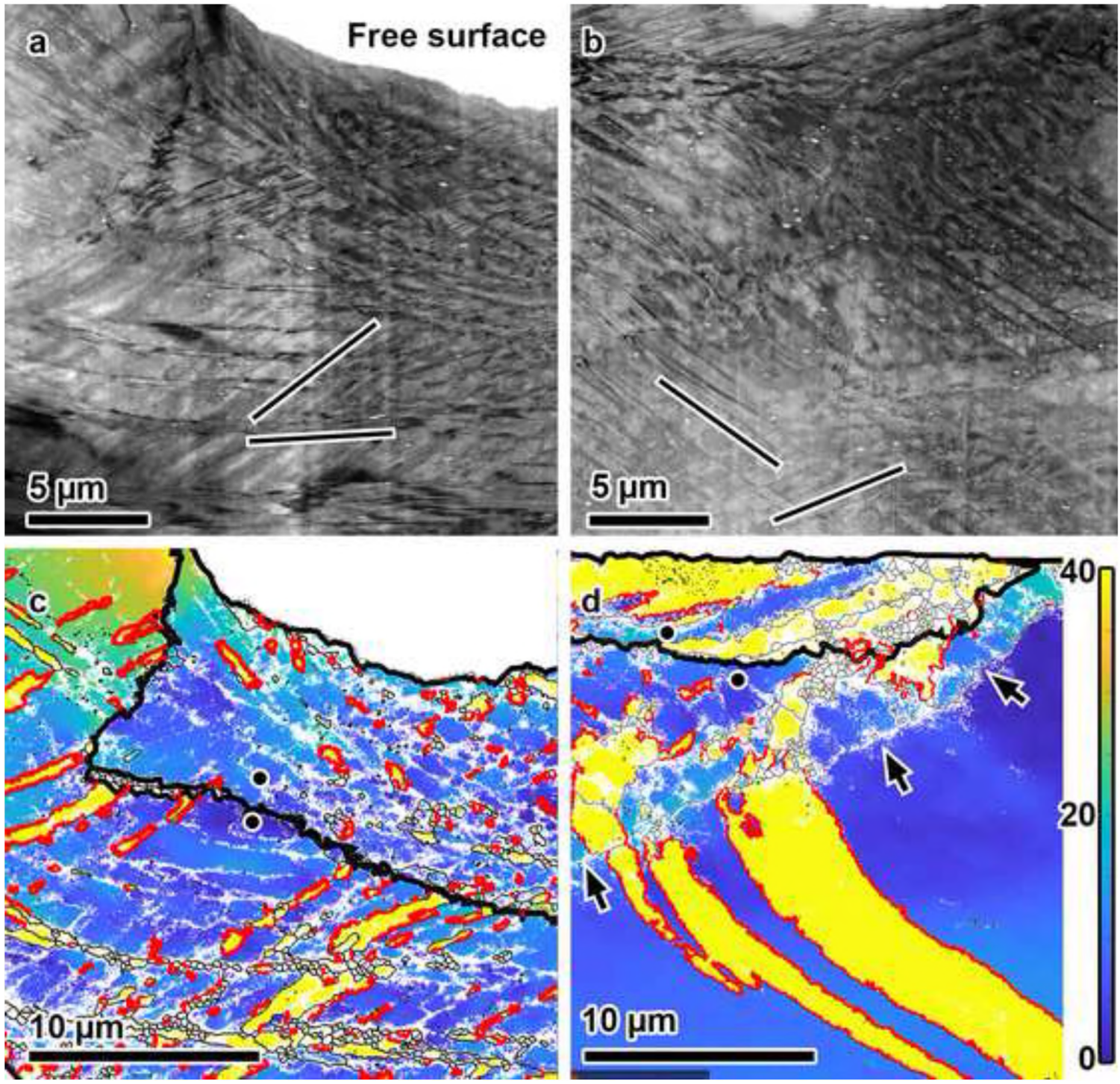


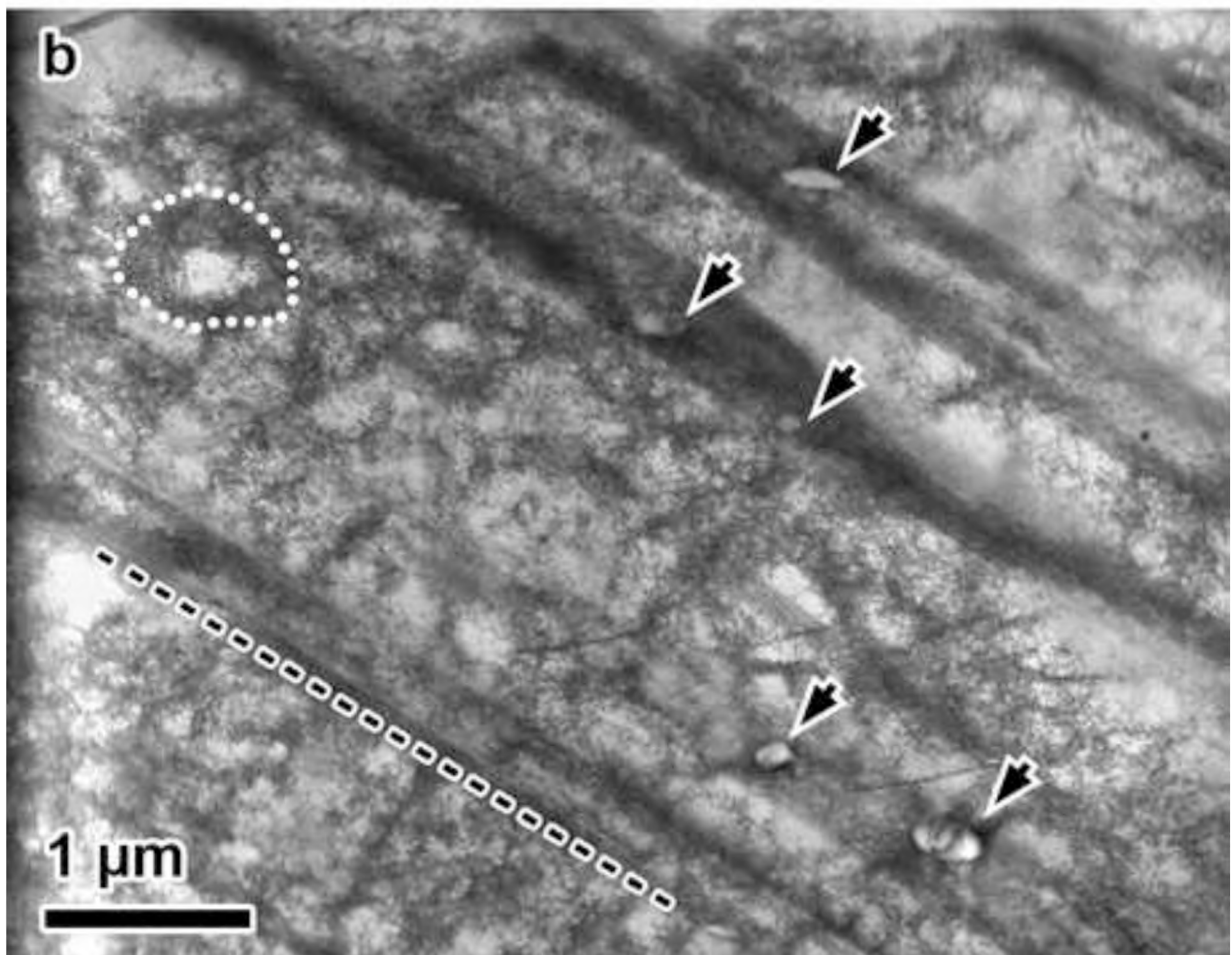
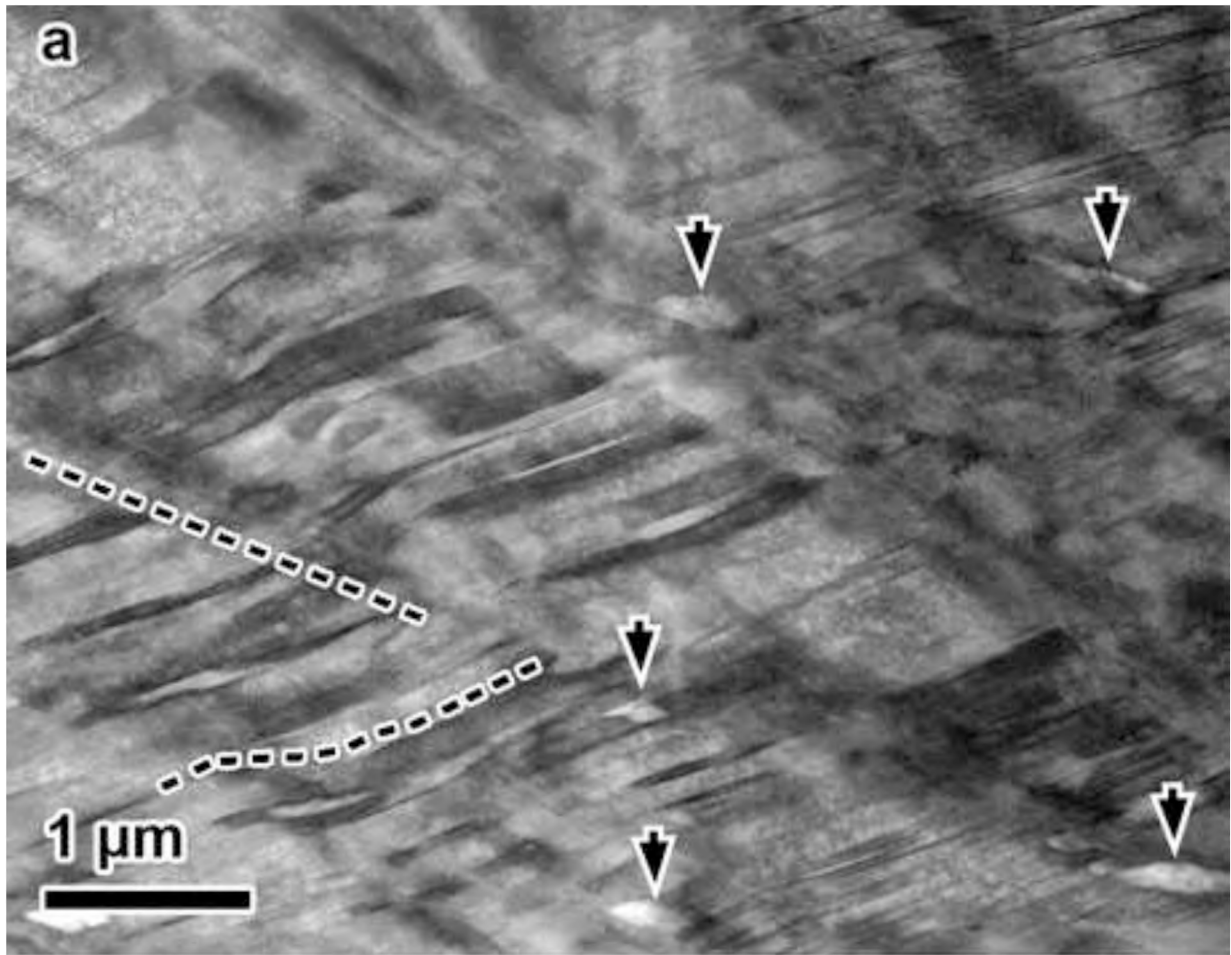


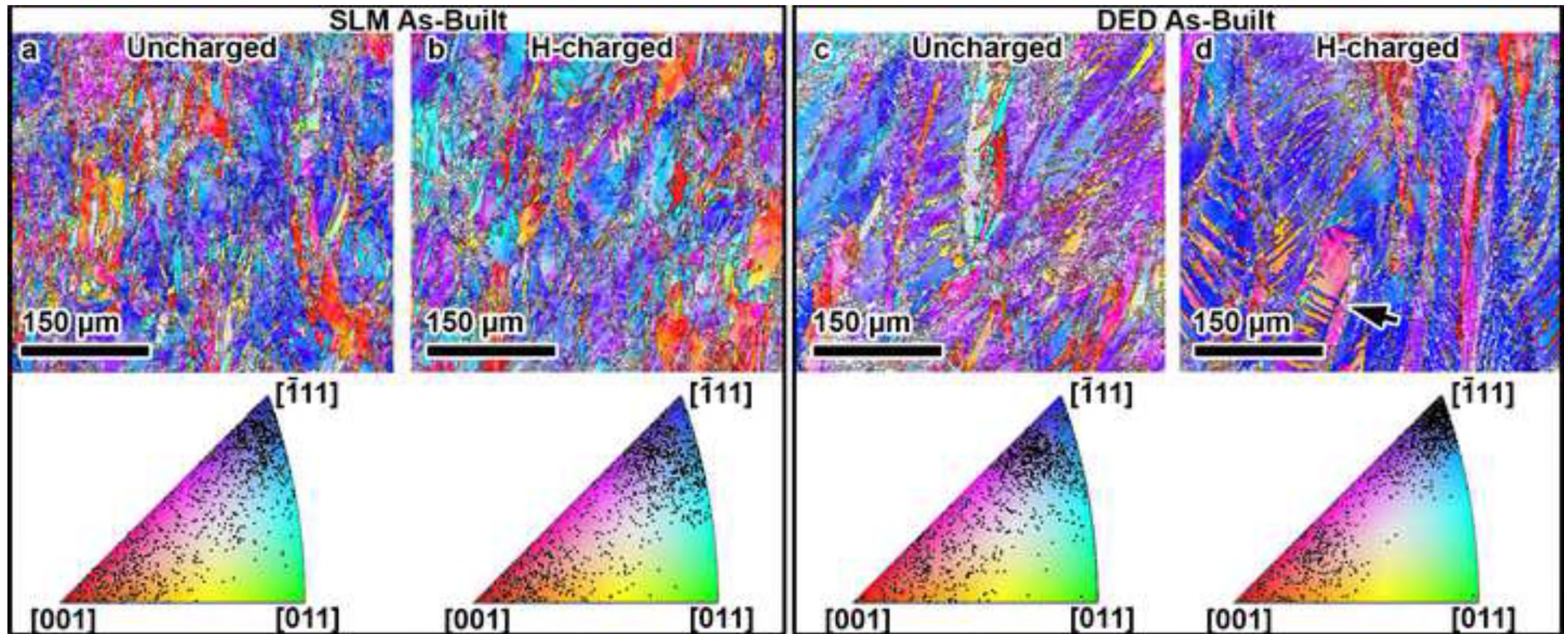












Declaration of interests

The authors declare that they have no known competing financial interests or personal relationships that could have appeared to influence the work reported in this paper.

The authors declare the following financial interests/personal relationships which may be considered as potential competing interests:

CRedit Author Statement

Kaila M. Bertsch: Conceptualization, Methodology, Validation, Formal analysis, Visualization, Investigation, Writing – Original Draft, Writing – Review & Editing

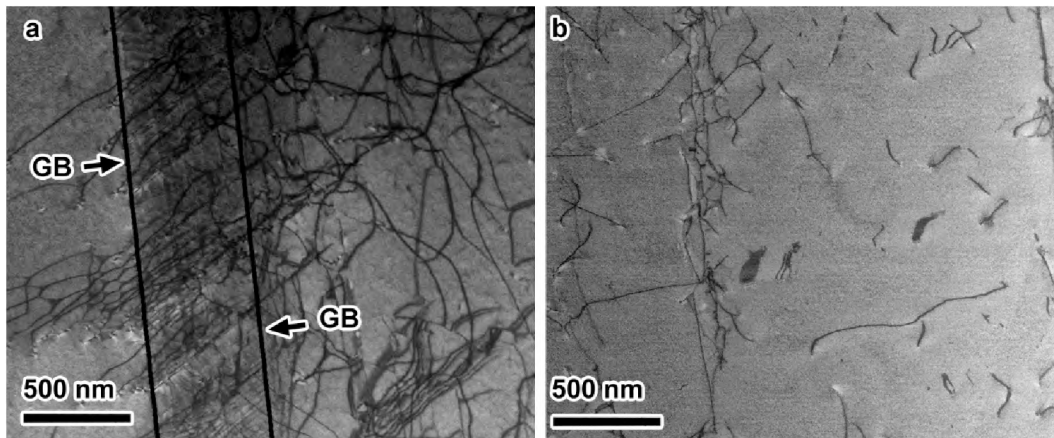
Akihide Nagao: Methodology, Investigation, Formal analysis, Visualization, Resources, Writing – Review & Editing

B. Rankouhi: Methodology, Investigation, Validation, Formal analysis, Investigation, Visualization, Writing – Review & Editing

B. Kuehl: Formal analysis, Sample preparation

D. J. Thoma: Funding acquisition, Project administration, Resources, Supervision, Validation, Writing – Review and Editing

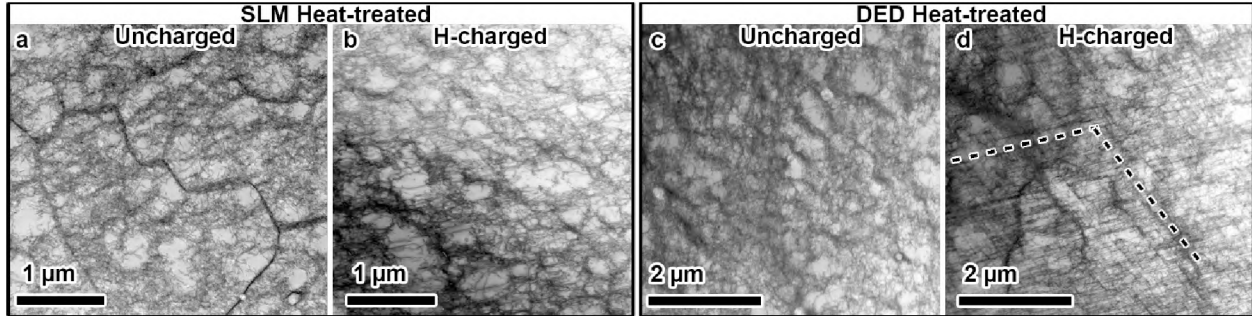
Dislocation Density in DED Heat-Treated Material



Supplemental Figure 1. Bright-field STEM of dislocation structures a. near a grain boundary inclined to the viewing plane, and b. in grain interiors in heat-treated material. The edge of the grain boundary is indicated by the straight black lines that are marked with arrows labeled GB in a.

Dislocation density was calculated from TEM images as detailed in [2]. In DED heat-treated material, grain boundaries tended to lie in extended planar configurations, without the high local curvature typical of dendritic structures, unlike boundaries in the as-built DED material. The highest dislocation densities were found within approximately 2-5 μm of grain boundaries, otherwise known as the grain boundary mantle region, where dislocations typically formed organized pileups, extended planar dislocations, or hexagonal networks, as shown in Supplemental Fig. 1a for the region surrounding a planar grain boundary inclined to the foil surface. The edge of the boundary is indicated by the straight black lines that are marked with arrows labeled GB. The dislocation density in the mantle region was approximately $4.7 \times 10^{13} \text{ m}^{-2}$. In the grain interiors, dislocations were sparser and more isolated, as shown in Supplemental Fig. 1b. The dislocation density in the grain interiors was approximately $2.7 \times 10^{13} \text{ m}^{-2}$. To estimate the overall dislocation density, the area fraction of grain boundaries and grain boundary mantles was calculated from EBSD maps to be 28.4%, and a weighted average of the dislocation density in the mantle regions and the grain interiors was taken, yielding an approximate dislocation density of $3.3 \times 10^{13} \text{ m}^{-2}$ overall. Segregation was not observed.

Microstructures of Heat-Treated SLM and DED Materials at Intermediate Strain



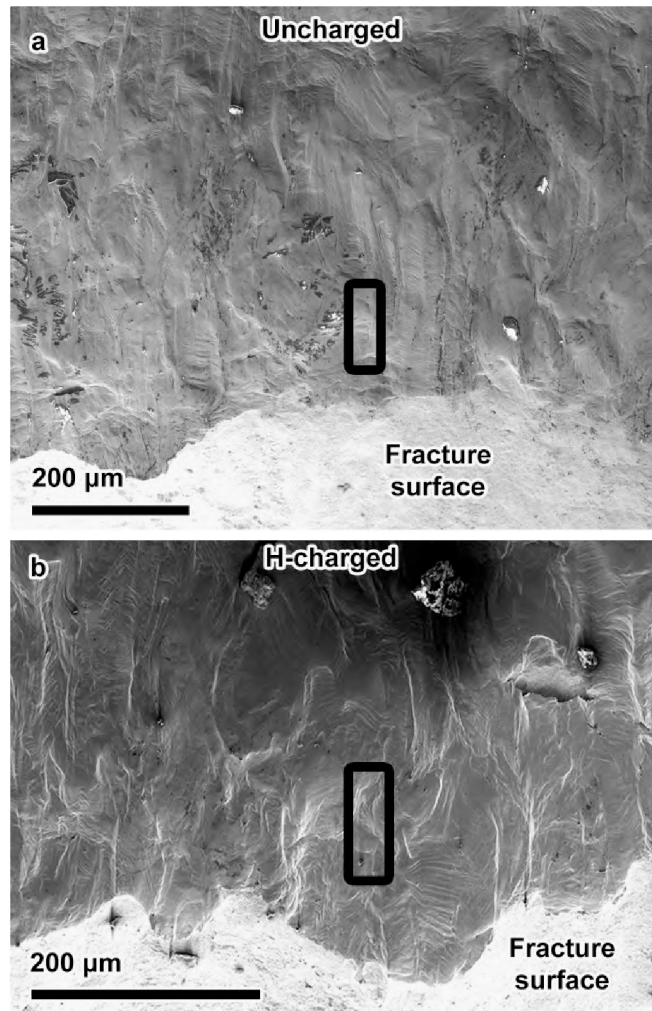
Supplemental Figure 2. Bright-field STEM micrographs of dislocation structures at 15% elongation in a,b. SLM heat-treated, and c,d. DED heat-treated materials. Dashed lines in d. indicate planar slip systems on $\{111\}$ planes.

In heat-treated SLM material that was interrupted at 15% elongation, dislocations had begun to organize into loosely-defined walls and tangles, as shown in Supplemental Fig. 2a and b. The initial dislocation structure was sparse and disorganized, with tangles but not cells or defined walls [1]. Thus, at 15% elongation, refinement of the defect microstructure had occurred. The presence of hydrogen did not appear to influence the dislocation structure organization in SLM heat-treated material, as shown in Supplemental Fig. 2b. Deformation twinning was not observed in these materials.

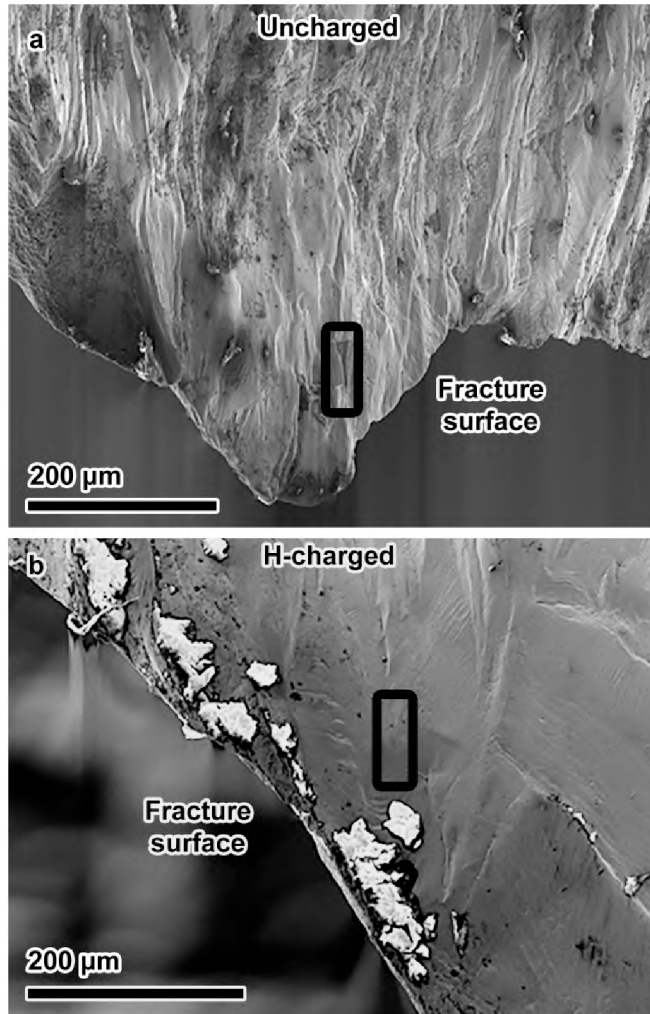
Hydrogen had the largest effect on the development of plasticity in the heat-treated DED material that was interrupted at 15% elongation. In the uncharged heat-treated DED material, dislocation tangles and walls had begun to form as shown in Supplemental Fig. 2c and d, with a random, equiaxed nature similar to that observed in the heat-treated SLM material. In the hydrogen-charged heat-treated DED material, Supplemental Fig. 2d, tangles were observed, but structures had become substantially more planar, lying type crystallographic planes. Examples of the planar, $\{111\}$ -type dislocation structures are indicated parallel to the dashed lines in Supplemental Fig. 2d.

Enhanced slip planarity in the presence of hydrogen has been well-documented in many FCC materials [3-5]. The current results appear to indicate that this effect is dependent on the initial microstructure of the material, since enhanced planarity in the presence of hydrogen was only notably observed in the heat-treated DED material. However, this is not considered to have a significant influence on the tensile properties, since hydrogen was not observed to have a deleterious effect on tensile properties in DED heat-treated material. Deformation twinning was not initiated in the uncharged or hydrogen-charged heat-treated DED material at 15% strain.

Locations of Regions Extracted via FIB for TEM Microstructural Analysis near Fracture Surfaces



Supplemental Figure 3. SEM images of free surfaces adjacent to fracture surfaces in a. uncharged and b. hydrogen-charged as-built SLM materials. Black boxes outline approximate location of regions extracted via FIB machining for S/TEM and t-EBSD analyses. Tensile axis is vertical.

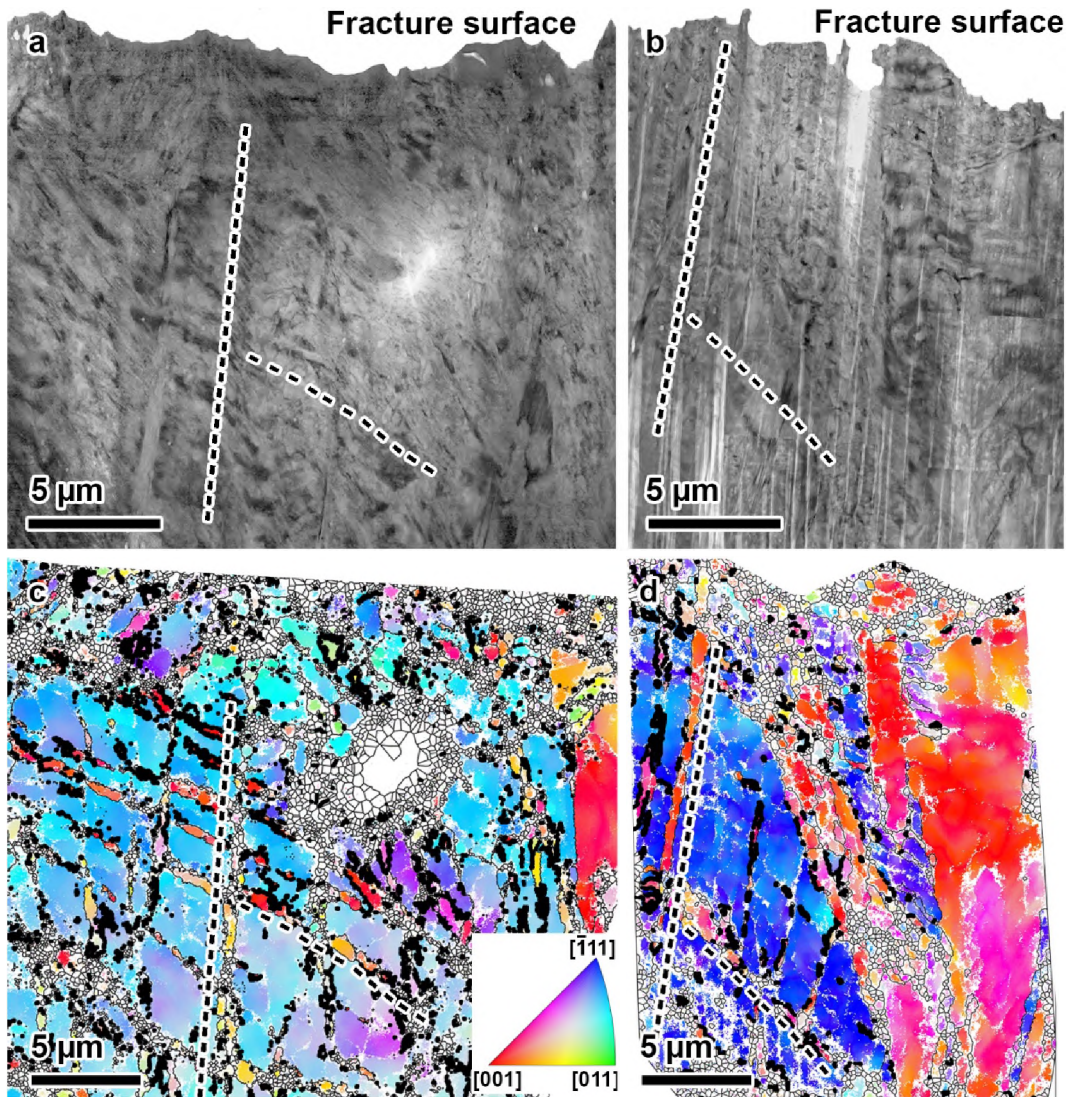


Supplemental Figure 4. SEM images of free surfaces adjacent to fracture surfaces in a. uncharged and b. hydrogen-charged as-built DED material. Black boxes outline approximate location of regions extracted via FIB machining for S/TEM and t-EBSD analyses. Tensile axis is vertical.

Microstructures beneath Fracture Surfaces

The microstructures beneath fracture surfaces are shown in Supplemental Figs. 5-8. In Supplemental Fig. 5, as-built SLM material is shown. In uncharged as-built SLM material, fracture surface microstructures consisted of subgrain bands approximately 200-500 nm wide spaced 500 nm - 4 μm apart, deformation twin bundles, and dense dislocation tangles, but no martensite, as illustrated in the STEM image in Supplemental Fig. 5a and the corresponding t-EBSD map in Supplemental Fig. 5c. Dashed lines in Supplemental Fig. 5a and c highlight corresponding subgrain bands. In Supplemental Fig. 5c, points were colored according to their crystallographic orientation with respect to the loading axis (vertical); red or yellow bands within the larger blue grain represent subgrain bands in multiple directions. The spacing of these subgrain bands was varied and they were multidirectional, such that it was not possible to correlate any sets of bands directly with the initial elongated dislocation cell structures. Local boundaries with misorientation 3° or greater were plotted as thin black lines, while twin bundles were plotted as thicker black lines.

Points with low confidence index are shown in white and were excluded from the analysis. Due to the high levels of strain, indexing of the backscattered Kikuchi patterns was not straightforward leading to a relatively high proportion of low-confidence-index points in fracture surface specimens. This led to the appearance of many small/single-pixel grains in some regions, for example near the top of Supplemental Fig. 5c and d. TEM imaging was used to confirm the absence of martensite, actual locations of subgrains, and presence of twins in these locations.

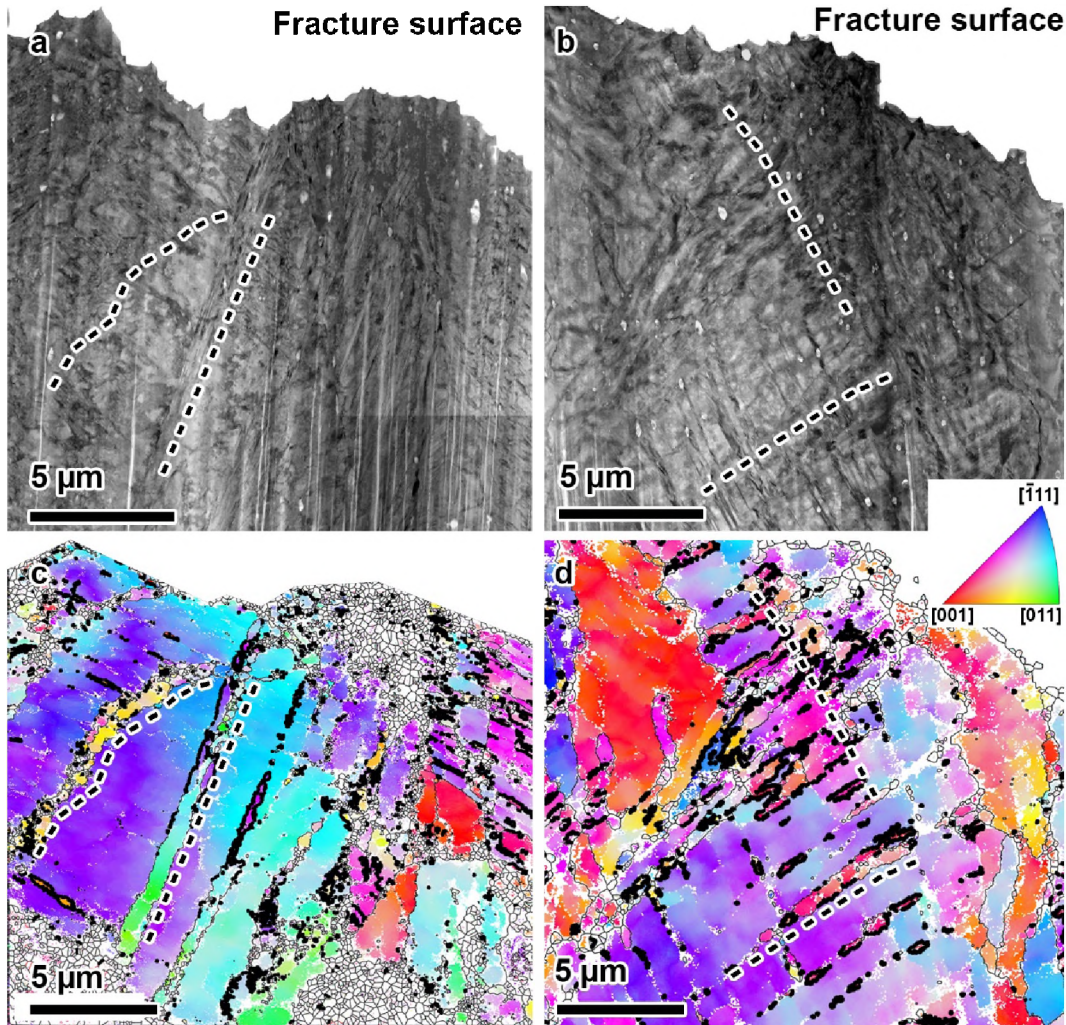


Supplemental Figure 5. Bright-field STEM micrographs (top row) and t-EBSD orientation maps (bottom row) of microstructures beneath the fracture surfaces in a, c. uncharged as-built SLM material and b, d. hydrogen-charged as-built SLM material. Dashed lines indicate subgrain bands. In c, d., thin black lines show local boundaries with misorientation 3° or greater. Thick black lines indicate twin boundaries. Orientation maps colored according to the crystallographic orientation in the tensile direction (vertical). Color online.

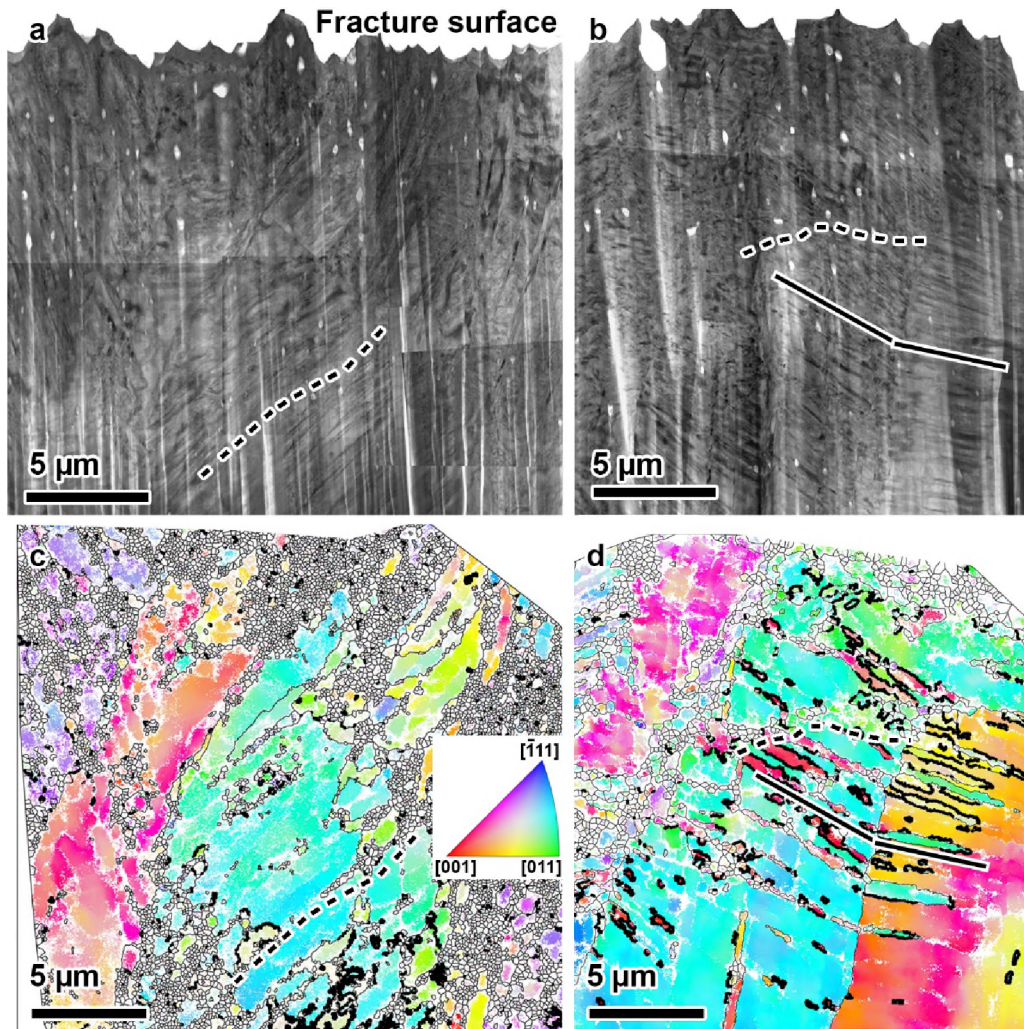
In hydrogen-charged as-built SLM material, a similar subgrain structure was observed, as indicated parallel to the dashed lines in Supplemental Fig. 5b and d. The width and spacing of these bands were in the same range as those observed in the uncharged as-built SLM material. As in the uncharged case, slightly over half of the identified bands were found to comprise twin bundles. In summary, little difference was observed in the deformation patterns beneath the fracture surfaces in hydrogen-charged compared to uncharged as-built SLM material.

Deformation mechanisms were similar in all other materials, exhibiting subgrain bands, deformation twins, and dense dislocation structures; strain-induced martensite was not detected in any of the areas interrogated. Subsurface microstructures for other alloys are shown in Supplemental Figs. 6-8. Hydrogen was generally not observed to significantly affect the subsurface deformation microstructures within $25\ \mu\text{m}$ of the fracture surface, which may be attributed to the final microvoid coalescence process eliminating preexisting defect structures

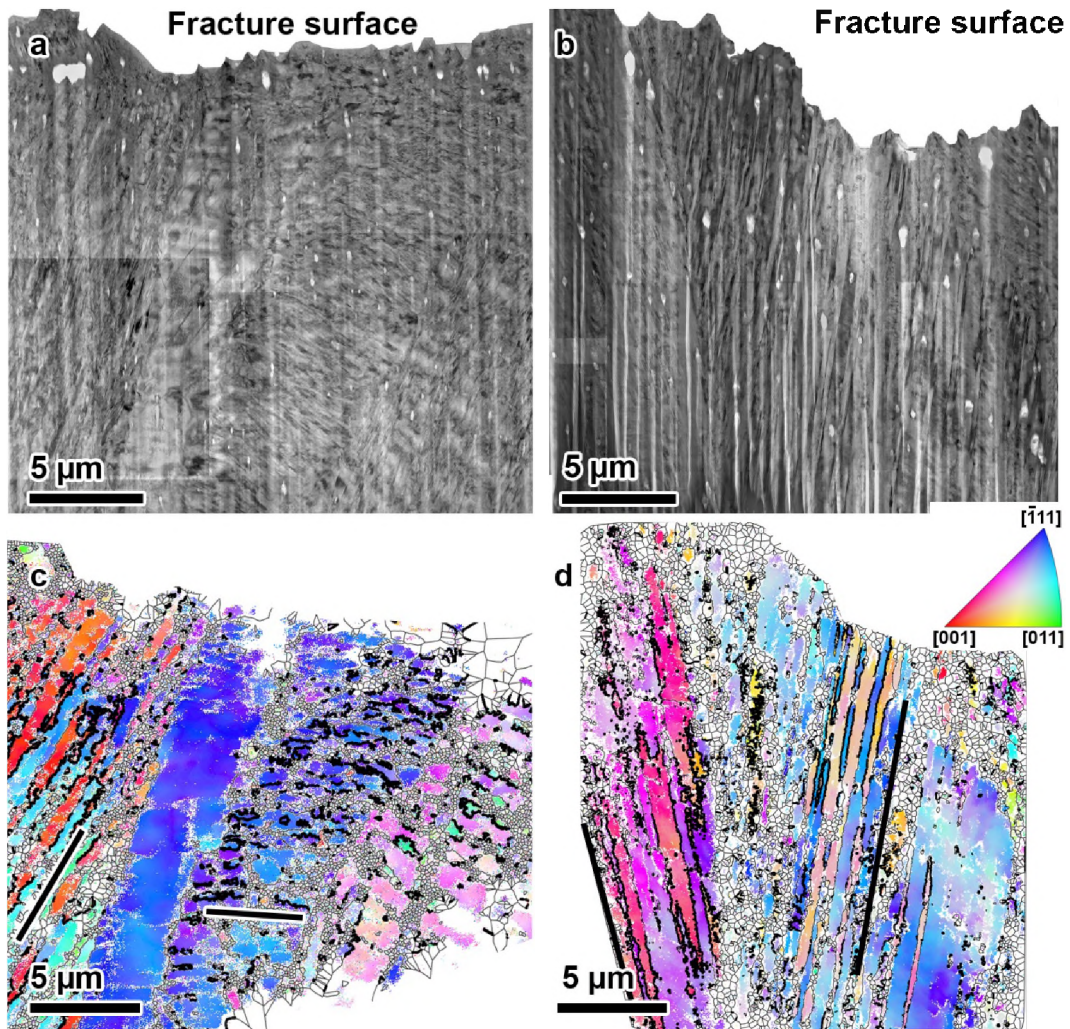
[6]. In as-built DED material, curved deformation bands were observed to be more defined near grain boundaries, Supplemental Fig. 7. However, the limited sample size makes it difficult to discern whether this feature is general or a function of the specific grains interrogated.



Supplemental Figure 6. Bright-field STEM micrographs (top row) and t-EBSD orientation maps (bottom row) of microstructures beneath the fracture surfaces in a, c. uncharged heat-treated SLM and b, d. hydrogen-charged heat-treated SLM materials. In c, d., thin black lines indicate local misorientations of 3° or greater. Thick black lines indicate twins. Dashed lines indicate subgrain bands. Color online.



Supplemental Figure 7. Bright-field STEM micrographs (top row) and t-EBSD orientation maps (bottom row) of microstructures beneath the fracture surfaces in a, c. uncharged as-built DED material and b, d. hydrogen-charged as-built DED material. In c, d., thin black lines indicate local misorientations of 3° or greater. Thick black lines indicate twins. Dashed lines indicate subgrain bands. Color online.



Supplemental Figure 8. Bright-field STEM micrographs (top row) and t-EBSD orientation maps (bottom row) of microstructures beneath the fracture surfaces in a, c. uncharged heat-treated DED material and b, d. hydrogen-charged heat-treated DED material.

In c, d., thin black lines indicate local misorientations of 3° or greater. Thick black lines indicate twins. Dashed lines indicate subgrain bands. Color online.

References

- [1] B. Rankouhi, K.M. Bertsch, G. Meric de Bellefon, M. Thevamaran, D.J. Thoma, K. Suresh, Experimental validation and microstructure characterization of topology optimized, additively manufactured SS316L components, *Mater. Sci. Eng. A* 776 (2020) 139050.
<https://doi.org/10.1016/j.msea.2020.139050>.
- [2] K.M. Bertsch, G. Meric de Bellefon, B. Kuehl, D.J. Thoma, Origin of dislocation structures in an additively manufactured austenitic stainless steel 316L, *Acta Mater.* 199 (2020) 19-33.
<https://doi.org/10.1016/j.actamat.2020.07.063>.
- [3] P.J. Ferreira, I.M. Robertson, H.K. Birnbaum, Influence of hydrogen on the stacking-fault energy of an austenitic stainless steel, *Mater. Sci. Forum* 93 (1996) 207.
[10.4028/www.scientific.net/MSF.207-209.93](https://www.scientific.net/MSF.207-209.93).
- [4] P.J. Ferreira, I.M. Robertson, H.K. Birnbaum, Hydrogen effects on the character of dislocations in high-purity aluminum, *Acta Mater.* 47 (1999) 2991.
[https://doi.org/10.1016/S1359-6454\(99\)00156-1](https://doi.org/10.1016/S1359-6454(99)00156-1).
- [5] I.M. Robertson, M.L. Martin, J.A. Fenske, Influence of hydrogen on the behavior of dislocations, in: R.P. Gangloff, B.P. Somerday (Eds.), *Gaseous Hydrogen Embrittlement of Materials in Energy Technologies*, Woodhead Publishing, 2012, pp. 166-206.
<http://doi.org/10.1533/9780857095374.1.166>.
- [6] D.W. Gross, The microstructural evolution of fatigue cracks in fcc metals, Ph.D. thesis, *Mater. Sci. Eng.*, University of Illinois at Urbana-Champaign (2016).